GRADUATE AERONAUTICAL LABORATORIES
CALIFORNIA INSTITUTE OF TECHNOLOGY

Turbulent mixing in transverse jets

Jerry W. Shan and Paul E. Dimotakis

September 2001

Report CaltechGalcitFM:2001.006

Firestone Flight Sciences Laboratory

Guggenheim Aeronautical Laboratory

Karman Laboratory of Fluid Mechanics and Jet Propulsion

Pasadena

Turbulent mixing in transverse jets

Jerry W. Shan and Paul E. Dimotakis

Graduate Aeronautical Laboratories
California Institute of Technology
Pasadena, CA 91125

Turbulent mixing is studied in liquid-phase transverse jets. Jet-fluid concentration fields were measured using laser-induced fluorescence and digital-imaging techniques, for jets in the Reynolds number range $1.0 \times 10^3 \leq Re_\mathrm{j} \leq 20 \times 10^3$, at a jet-to-freestream velocity ratio $V_\mathrm{r} = 10$. Analysis of the measured scalar fields indicates that turbulent mixing is Reynolds-number dependent, as manifest in the evolving probability density functions of jet-fluid concentration. Enhanced homogenization is found with increasing Reynolds number. Turbulent mixing is also seen to be flow dependent, based on differences between jets discharging into a crossflow and jets into a quiescent reservoir. A novel technique for whole-field measurement of scalar increments was used to study the distribution of difference (scalar increments) of the scalar field. These scalar increments are found to tend toward exponential-tailed distributions with decreasing separation distance. Finally, the scalar field is found to be anisotropic, particularly at small length scales. This is seen in power spectra, directional scalar microscales, and directional PDFs of scalar increments. The local anisotropy of the scalar field is explained in terms of the global dynamics and large-scale strain field of the transverse jet.

1. Introduction

The turbulent jet discharging into a crossflow, or transverse jet, is a turbulent free-shear flow with both environmental and technological significance. For instance, thermal plumes generated near ground level by volcanoes, thunderstorms, or forest fires can often rise to heights in the atmosphere where significant crossflow exists. A familiar occurrence of transverse jets is when a plume is emitted from a smokestack into a crosswind. Other situations in which transverse jets arise include effluent discharge from sewage-treatment plants into rivers, steering jets, VTOL/STOL aerodynamics, and blade-and-endwall cooling in gas-turbine engines. Transverse jets have recently been proposed as a means for fuel injection in high-speed, air-breathing propulsion devices, such as SCRAMJETS (*e.g.*, Mathur *et al.*

CaltechGalcitFM:2001.006

1999). Many of the examples discussed have buoyancy effects to varying degree; however, buoyancy-driven transverse jets appear to be similar in structure and share many characteristics with momentum-driven transverse jets.

Early studies of transverse jets focused on jet trajectories, mean velocity fields, and cross-sectional shapes (Keffer & Baines 1963, Kamotani & Greber 1972, Chassaing *et al.* 1974). A persistent, counter-rotating vortex pair in the far field of the transverse jet was noted in numerous experiments (Keffer & Baines 1963, Fearn & Weston 1974). Periodic motion in the wake of the transverse jet was found by Gordier (1959), McAllister (1968), and Reilly (1968), and characteristic Strouhal frequencies were measured by McMahon *et al.* (1971) and Moussa *et al.* (1977). Vortices in the wake of a turbulent jet issuing transversely to a freestream were first visualized by Kuzo & Roshko (1984). The origin of these wake vortices was studied in detail by Fric & Roshko (1994). Renewed interest in the structure and dynamics of vorticity in transverse jets led to work by Kelso & Smits (1995), Morton & Ibbetson (1996), and Kelso *et al.* (1996). In 1984, Broadwell & Breidenthal modeled the counter-rotating vortex pair as a global consequence of the normal momentum imparted by the jet to the freestream. Karagozian (1986) studied the vorticity associated with a transverse jet and modeled jet trajectories, mean vortex-pair strength, and reaction lengths. Kuzo (1995) reported, based upon particle-image-velocimetry measurements, that the mean flow state in the far field of the transverse jet is not necessarily a symmetric vortex pair, but can be unsteady and asymmetric under certain conditions. A comprehensive review of jet-in-crossflow research was presented by Margason (1993).

The scalar field of transverse jets has received somewhat less attention than the velocity and vorticity fields. Mean scalar fields were experimentally measured by Andreopoulos & Rodi (1984) and Niederhaus *et al.* (1997). Large-eddy simulations have been conducted by Yuan *et al.* (1999), among others. Cortelezzi & Karagozian (2001) computed the formation of the counter-rotating vortex pair in the near field of transverse jets using three-dimensional vortex elements. The vortex interaction region, mean trajectories and concentration decay, and overall structural features of mixing were studied by Smith & Mungal (1998). Yet, as noted by Niederhaus *et al.* (1997), "...the vast majority of the published work [on transverse jets] has focused on issues concerning the velocity field. Remarkably, there is a scarcity of research directed toward scalar transport or mixing, even though the majority of applications require knowledge of the transport of either mass or heat."

The results of experiments measuring scalar fields in turbulent transverse jets

are described in this paper. These measurements have enabled analysis of many aspects of turbulent mixing. In particular, Reynolds-number effects on mixing, the flow-dependence of turbulent mixing, and the anisotropy of scalar fields are discussed. Section 2 shows sample image data, and gives details of the experimental procedure and imaging technique. A three-dimensional, space-time visualization of the transverse jet is depicted in Sec. 3. In Sec. 4, the viscous-dissipation and scalar-diffusion scales for the transverse jet are estimated. Classical measures of turbulent jets, such as trajectories, concentration decay, and power spectra, are presented in Sec. 5. Section 6 describes the scalar field, and Reynolds-number effects on turbulent mixing, in terms of probability-density functions (PDFS) of jet-fluid concentration. Comparison is made between mixing in transverse jets, and turbulent jets discharging into a quiescent reservoir. In Sec. 7, the distribution of differences of the scalar field is considered. A technique for whole-field measurements of scalar increments is introduced, and PDFs of scalar increments are computed in the far-field of the transverse jet. Section 8 discusses direction-dependent scalar microscales, and quantifies scalar-field anisotropy as a function of Reynolds number. Section 9 proposes an explanation for the observed anisotropy of the scalar field in transverse jets.

2. Experiments and imaging technique

Experiments on liquid-phase, turbulent transverse jets were conducted in the GALCIT Free-Surface Water Tunnel (FSWT), a closed-circuit facility with a 20 in (0.508 m) -wide $\times$ 30 in (0.762 m) -deep test section. For these experiments, the FSWT was operated as a water tunnel with a square test section by maintaining the test-section water level at a depth of 20 in, and fitting a surface plate flush with the top of the water (Fig. 1). Jet flow was injected perpendicular to the freestream by air-pressurizing an inverted, liquid-filled plenum that was mounted on top of the surface plate. The jet nozzle was convex contoured to suppress the formation of Görtler instabilities, and had an area-contraction ratio of 43. The freestream velocity in the test section was monitored with laser-doppler velocimetry, while the jet velocity was set by choosing a predetermined, calibrated, driving pressure. Experiments were conducted at several different Reynolds numbers, $Re_{\rm j} \equiv U_{\rm j} d_{\rm j}/\nu$ = 1.0, 2.0, 5.0, 10, and 20 $\times$ 10^3, where $U_{\rm j}$ is the mean jet-exit velocity, $d_{\rm j}$ is the nozzle diameter, and ν is the kinematic viscosity of water. The jet-to-freestream velocity ratio investigated was $V_{\rm r} \equiv U_{\rm j}/U_\infty = 10$. Experiments were also performed at $V_{\rm r} = 32$, but only for visualization purposes. The data analyzed for this paper are for $V_{\rm r} = 10$ jets.

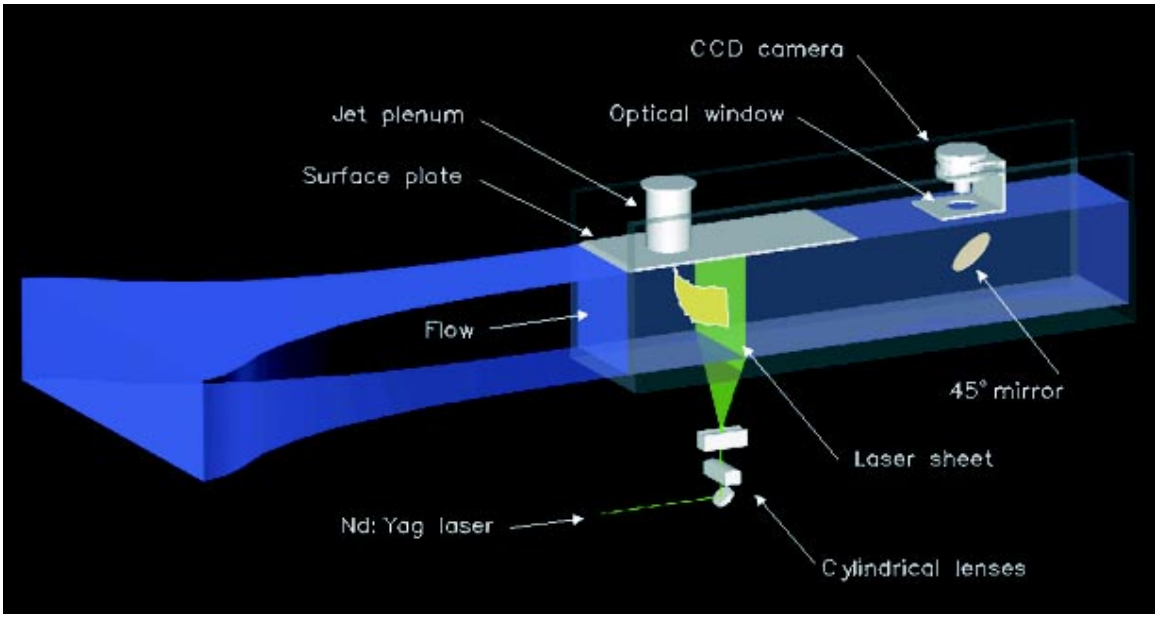

FIG. 1 Experimental facility and imaging configuration for transverse sections of transverse jet, measured at downstream location $x/d = 50$.

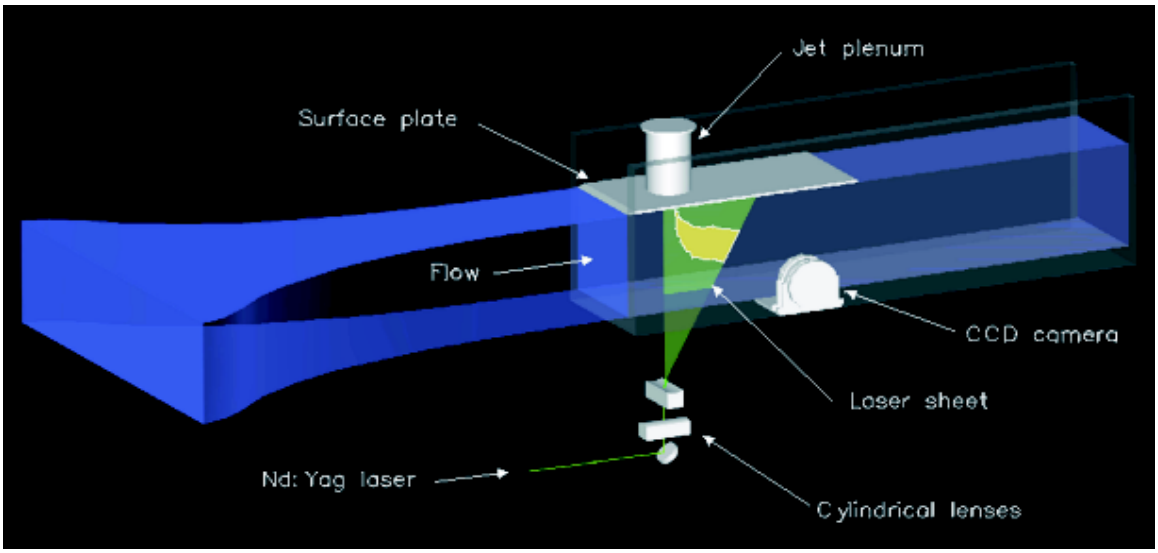

FIG. 2 Experimental facility and imaging configuration for streamwise sections of transverse jet.

Laser-induced fluorescence (LIF) and digital imaging techniques were used to measure jet-fluid concentration fields. Water in the jet plenum was seeded with fluorescent dye, rhodamine-6G chloride, in molar concentrations between 1.4×10^{-6} and 1.4×10^{-5}. When excited with a frequency-doubled, Q-switched Nd:YAG laser (Continuum YG661), the jet fluid fluoresced, while undyed tunnel fluid remained

dark. For rhodamine-6G in water, the absorption and fluorescence-emission peaks are $\lambda = 526$ nm and 555 nm, respectively (Pringsheim 1949), while the Schmidt number, $Sc \equiv \nu/\mathcal{D}$, is estimated to be 8.4×10^3 (Axelrod *et al.* 1976, Walker 1987). The scalar diffuses less effectively than vorticity, and has smaller length scales than the vorticity field, as discussed in Sec. 4. A laser sheet was formed by directing the beam of Nd:YAG laser through a series of cylindrical lenses, which expanded the beam in one direction, while focusing it to a waist in another direction. The thickness of the laser sheet was less than 1 mm throughout the imaged field of view. Both streamwise and perpendicular slices of the scalar field of the transverse jet were recorded. Streamwise slices of the scalar field were measured on the centerline of the transverse jet, for a field of view of $53d_\mathrm{j} \times 53d_\mathrm{j}$ (Fig. 2). Transverse slices were measured at a downstream location $x/d_\mathrm{i} = 50$, and had a field of view of (31×31)-d_j (Fig. 1).

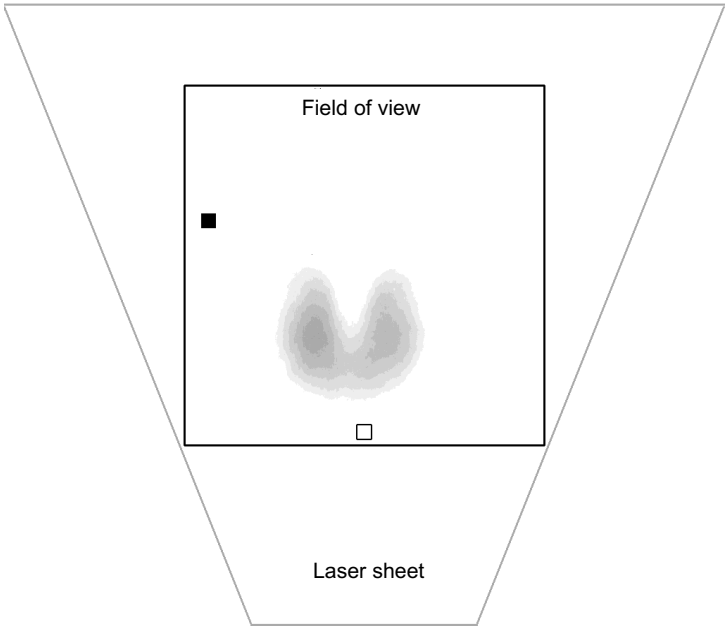

FIG. 3 Light sheet geometry (gray outline) and imaged field of view (dark outline), with superimposed mean jet-fluid concentration. Open box shows location of maximum laser sheet intensity, $I_{\mathrm{L,max}}$. Filled box box shows location of minimum laser intensity, $I_{\mathrm{L,min}}$.

The suitability of rhodamine-6G chloride and a pulsed Nd:YAG laser for quantitative concentration measurements was verified in a separate investigation. This was prompted by the work of Karasso and Mungal (1997), who reported that sodium

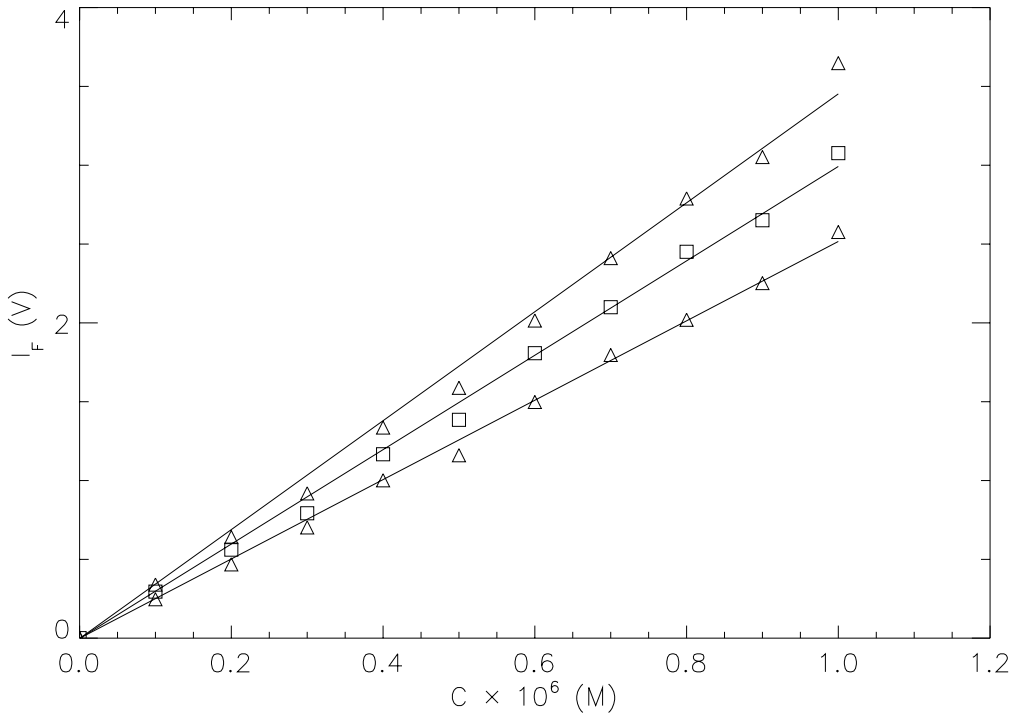

FIG. 4 Variation of fluorescence power with concentration. Fluorescence is linear with concentration, for three different laser intensities spanning the minimum and maximum range of intensities in the laser sheet.

fluorescein dye has non-linear fluorescence response when excited by the Nd:YAG laser. In particular, the fluorescence intensity, I_{F}, for rhodamine-6G chloride was studied for variations with concentration at different laser power levels, I_{L}. An optical-glass cuvette, 45 mm in height and 10 mm $\times$ 20 mm in cross-section, (Starna Cells) was filled with dye concentrations between $0.1\times10^{-6}M$ and $1.0\times10^{-6}M$, and excited at several different laser intensities. Attenuation due to absorption within the cell was negligible due to the short pathlength and low concentrations. The fluorescence response was measured with a photodiode and recorded using a digital data acquisition system (National Instruments). The experimental apparatus for these fluorescence measurements was based on a setup developed by D. Gargas (2000). For the transverse jet measurements, the laser-illumination intensity also varied because of the geometric expansion of the sheet and the non-uniform distribution of the laser beam (Fig. 3). The laser intensity differed by a factor of 1.5 within the spatial extent of the scalar field in the field of view. It reached a maximum of $I_{\mathrm{L,max}} \simeq 0.017$ J/cm^2, at the center of the lower edge of the imaged field of view, and a minimum of $I_{\mathrm{L,min}} \simeq 0.011$ J/cm^2, at the sides of the image, where jet fluid only occasionally may be found. Jet fluid never reaches the upper corners of the field of view. Fluorescence response was measured for three different laser inten-

sities, and ten dye concentrations. As Fig. 4 shows, the fluorescence intensity was linearly proportional to dye concentration, to within the concentration uncertainty. This was true for three different laser intensities that spanned the range of variation found in the laser sheet used in this experiment. Fluorescence data were measured for laser energy fluxes of $0.071, 0.046$, and 0.028 J/cm^2 per pulse, or equivalently, power fluxes of $7.1, 4.6$, and 2.8×10^6 W/cm^2. In all cases, the root-mean-square deviations from best linear fits, that were constrained to go through the origin, were less than 1%.

Images of the scalar (jet-fluid) concentration field were recorded at 10 frames/s with the 12-bit/pixel, (1024×1024)-pixel Cassini digital-imaging system. This system, designed and built by D. Lang and P. Dimotakis, in collaboration with S. A. Collins and M. Wadsworth of the Jet Propulsion Laboratory, utilizes a low-noise, high dynamic-range CCD sensor developed for NASA's Cassini spacecraft. Contiguous time-sequences of 254 images were recorded for streamwise sections of the jet, and 508 images for transverse sections. Experiments were performed in a darkened laboratory to minimize noise from ambient light and a Kodak #21 optical low-pass filter was used to block any residual laser light. Because fluorescence is linear with dye concentration (Fig. 4), the imaged intensity of fluorescence, $I_{\rm F}(x_1, x_2, t)$, of a time-varying concentration field, $c(x_1, x_2, t)$, may be written as,

$$I_{\rm F}(x_1, x_2, t) = g\left[I_{\rm L}(x_1, x_2), S(x_1, x_2)\right] c(x_1, x_2, t) + I_{\rm back}(x_1, x_2)\,, \qquad (1a)$$

where $g(I_{\rm L}, S)$ is a function of the local laser intensity, $I_{\rm L}(x_1, x_2)$, and the pixel-by-pixel sensitivity, $S(x_1, x_2)$, of the imaging system. $I_{\rm back}$ is the cumulative background level due to dark noise, offsets, *etc.* in the CCD camera. The imaged intensity for a reference, uniform-concentration, field, would be,

$$I_{\rm F,ref}(x_1, x_2) = g\left[I_{\rm L}(x_1, x_2), S(x_1, x_2)\right] c_{\rm ref} + I_{\rm back}(x_1, x_2)\,, \qquad (1b)$$

where $c_{\rm ref}$ is a known concentration. The jet-fluid concentration field, referenced to the known concentration, may then be computed by calibrating the raw fluorescence image data with uniform-concentration images, and background-illumination images (*cf.* Eq. 1),

$$\frac{c(x_1, x_2, t)}{c_{\rm ref}} \;=\; \frac{I_{\rm F,raw}(x_1, x_2, t) - \left\langle\, I_{\rm back}(x_1, x_2)\,\right\rangle}{\left\langle\, I_{\rm F,ref}(x_1, x_2)\,\right\rangle - \left\langle\, I_{\rm back}(x_1, x_2)\,\right\rangle}\;. \qquad (2a)$$

This result relies on linearity with respect to concentration, as demonstrated in Fig. 4, but is basically independent of the function $g(I, S)$. The concentration measurement does not depend on the functional relation between fluorescence and laser intensity. For the intensity range of this experiment, however, the fluorescence was nonetheless very nearly linear with respect to laser intensity, *i.e.*,

$$g(I_{\rm L}, S) \;=\; g_0(S) + (I_{\rm L} - I_0) g_1(S) \;+\; {\rm H.O.T.'s}\,,$$

where the higher order terms in the expansion are small (less than 0.5% r.m.s.). The offset, $g_0(S)$, is not small for the intensity range for this experiment. For streamwise slices of the transverse jet, the coordinates x_1, x_2 denote the streamwise, x, and vertical, y, directions, respectively (Figs. 5 & 6). For transverse slices of the transverse jet, x_1, x_2 denote the horizontal (spanwise), z, and vertical, y, directions, respectively (Figs. 7 & 8). The origin of the coordinate system is taken to be the jet-nozzle exit, forming a right-handed system, with x pointing in the direction of jet injection (downward), y aligned with the freestream flow, and z directed in the spanwise direction.

Background images, $I_{\rm back}(x_1, x_2)$, were recorded shortly before each run, with laser firing and optical low-pass filter on the camera lens, but without the fluorescent-dye-seeded jet. After each run, reference images, $I_{\rm F,ref}(x_1, x_2)$, were recorded by immersing a transparent Lucite container filled with well-mixed dye of known concentration, $c_{\rm ref}$, in the test section. Using these images, Eq. 2 provides a procedue for a pixel-by-pixel calibration that normalizes the collective effects of CCD-pixel sensitivity variation, laser-illumination nonuniformity, and the imaging-system optical transfer function. The imaged jet-fluid concentration was then referenced to the jet-plenum dye concentration, c_0, by scaling all values with $c_{\rm ref}/c_0$ to yield the normalized jet-fluid-concentration scalar values, C, *i.e.*,

$$0 \;\le\; C(x_1, x_2, t) \equiv \frac{c(x_1, x_2, t)}{c_0} = \frac{c(x_1, x_2, t)}{c_{\rm ref}} \, \frac{c_{\rm ref}}{c_0} \;\le\; 1 \;. \qquad (2b)$$

The jet-plenum dye concentration, c_0, and the reference concentration, $c_{\rm ref}$, are known when the dye solutions are mixed. $C = 1$ then refers to pure jet fluid, *e.g.*, at the jet exit, while $C = 0$ refers to pure tunnel fluid.

For streamwise sections of the jet, shot-to-shot variations in the output power of the pulsed laser were measured and normalized by monitoring the fluorescence-intensity fluctuations at the jet-exit. This was possible because c_0 was constant during the course of an experiment, and the jet exit was visible in the streamwise

images. For transverse sections, the jet exit is not visible in the images, so a fiber-optic probe was used to collect a small fraction of the laser output and direct the illumination to a test tube filled with a rhodamine-6G solution. The fluorescent sample was imaged in an unused corner of the CCD array, and shot-to-shot power fluctuations of the laser were normalized with this measurement.

Examples of the calibrated and normalized scalar-field data for streamwise sections of the transverse jet are shown in Fig. 5, for $Re_{\rm j} = 1.0 \times 10^3$, and in Fig. 6, for $Re_{\rm j} = 10 \times 10^3$. In the low-Reyolds-number situation, the jet remains laminar for several nozzle diameters before becoming unsteady and transitioning to turbulence. Transition occurs very close to the jet exit for higher Reynolds numbers. In all cases, but especially for the higher velocity ratio, thin filaments, or "fingers", of jet fluid are seen to extend from the body of the jet, toward the injection wall. These "fingers" in the wake of the transverse jet can be seen in both streamwise and transverse measurements of the scalar field. While it is known that jet fluid does not enter the wake of jet for velocity ratios less than 10 (Fric & Roshko 1994), these experiments suggest that jet fluid, and associated jet shear-layer vorticity, may be transported into the wake of the transverse jet for high velocity ratios.

3. Three-dimensional visualization

Level sets of jet-fluid-concentration, $C(\mathbf{x}, t) = C_{\rm iso}$, are geometrically complex, and important, for instance, to chemical reaction rates, and for fluid mixing on the molecular scale. Isolines (in two-dimensions), or isosurfaces (in three-dimensions), may be extracted from the measured scalar field, $C(\mathbf{x}, t)$. In this experiment, three-dimensional, space-time visualizations of the scalar field are produced by assembling a sequence of two-dimensional images. Under certain conditions, this space-time measurement is an approximation of the three-dimensional spatial structure of the scalar field.

A space-time visualization of the jet-fluid concentration level set is shown in Fig. 9 for the $Re_{\rm j} \simeq 1.0 \times 10^3$, $V_{\rm r} = 10.1$, transverse jet. One particular isosurface of the scalar field is highlighted by choosing a small range of jet-fluid concentrations to be opaque and reflecting. In this visualization, the structure of the transverse jet is dominated by kidney-shaped, counter-rotating vortices. Two large, counter-rotating vortices, and a smaller, tertiary vortex, are seen at this low Reynolds number. The rotation of this tertiary vortex is evident in the filaments of jet-fluid that wrap around it. Filaments of dye reach up, from middle of the counter-rotating vortex pair, and wrap around the tertiary vortex.

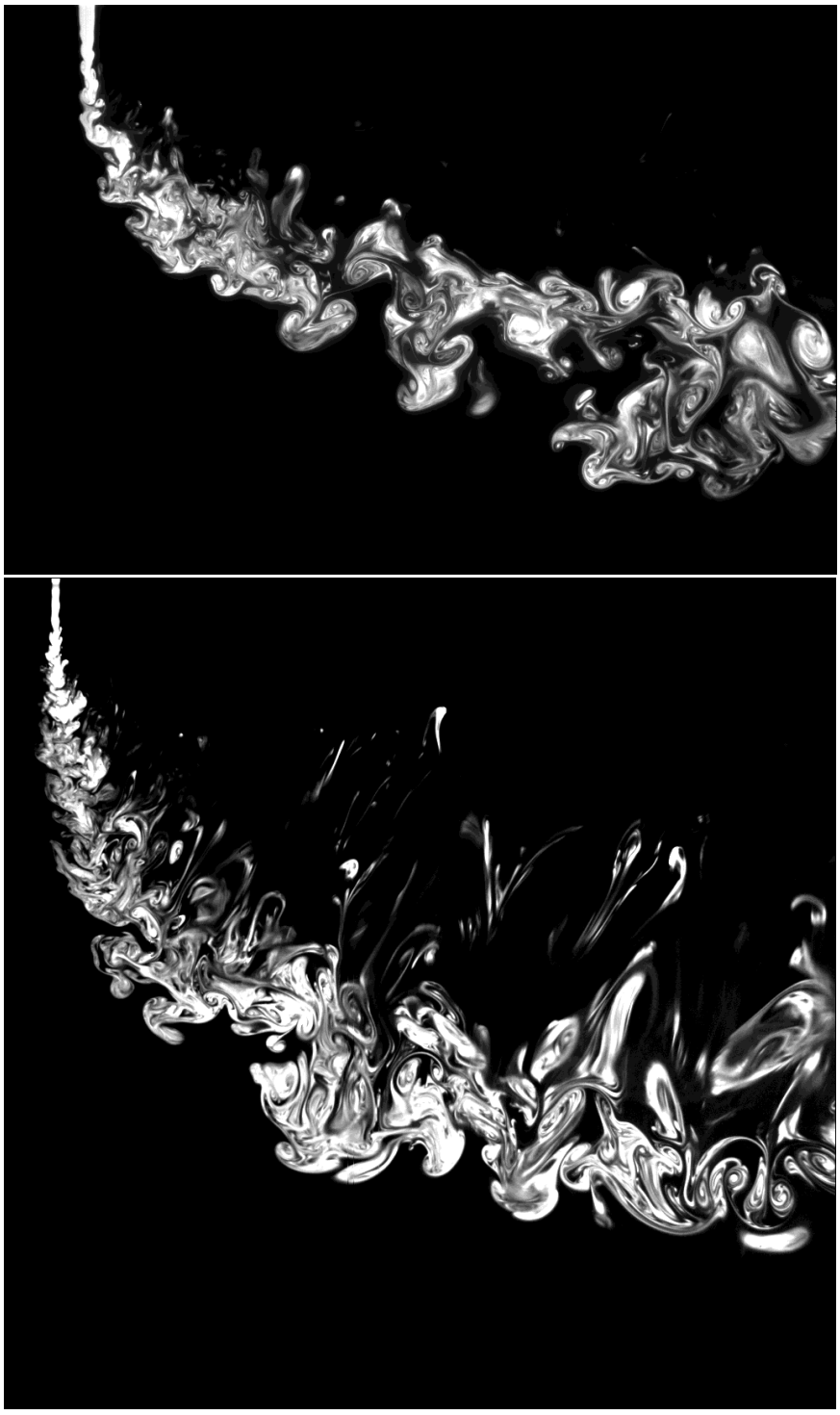

FIG. 5 Jet-fluid concentration in a streamwise, plane-of-symmetry slice of the transverse jet for $Re_{\mathrm{j}} = 1.0 \times 10^3$. Image data scaled by $x^{1/2}$ to compensate for downstream decay (for display purposes only). Top: $V_{\mathrm{r}} \simeq 10$. Bottom: $V_{\mathrm{r}} \simeq 32$.

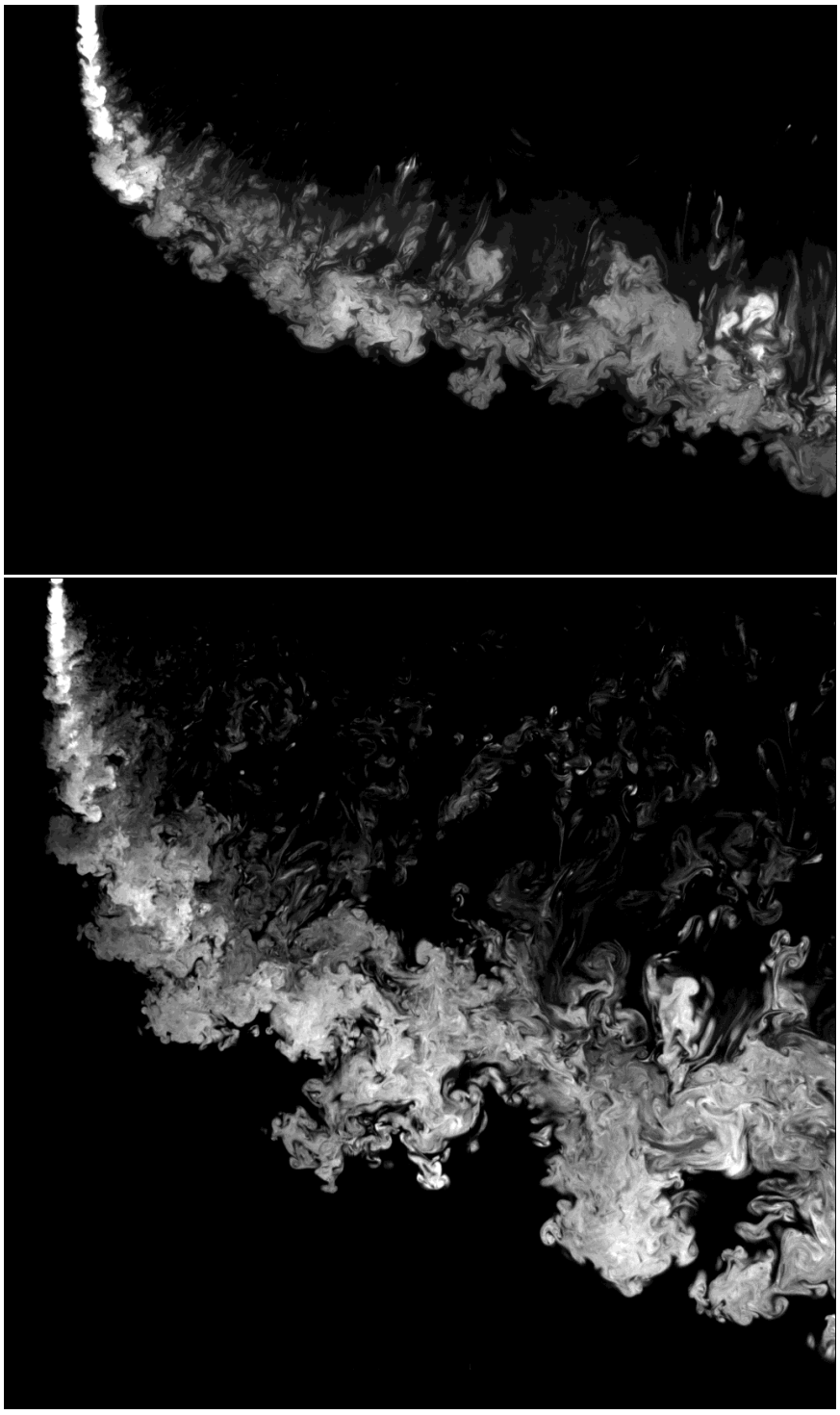

FIG. 6 Jet-fluid concentration in a streamwise, plane-of-symmetry slice of the transverse jet for $Re_{\rm j} = 10 \times 10^4$. Image data scaled by $x^{1/2}$ to compensate for downstream decay (for display purposes only). Top: $V_{\rm r} \simeq 10$. Bottom: $V_{\rm r} \simeq 32$.

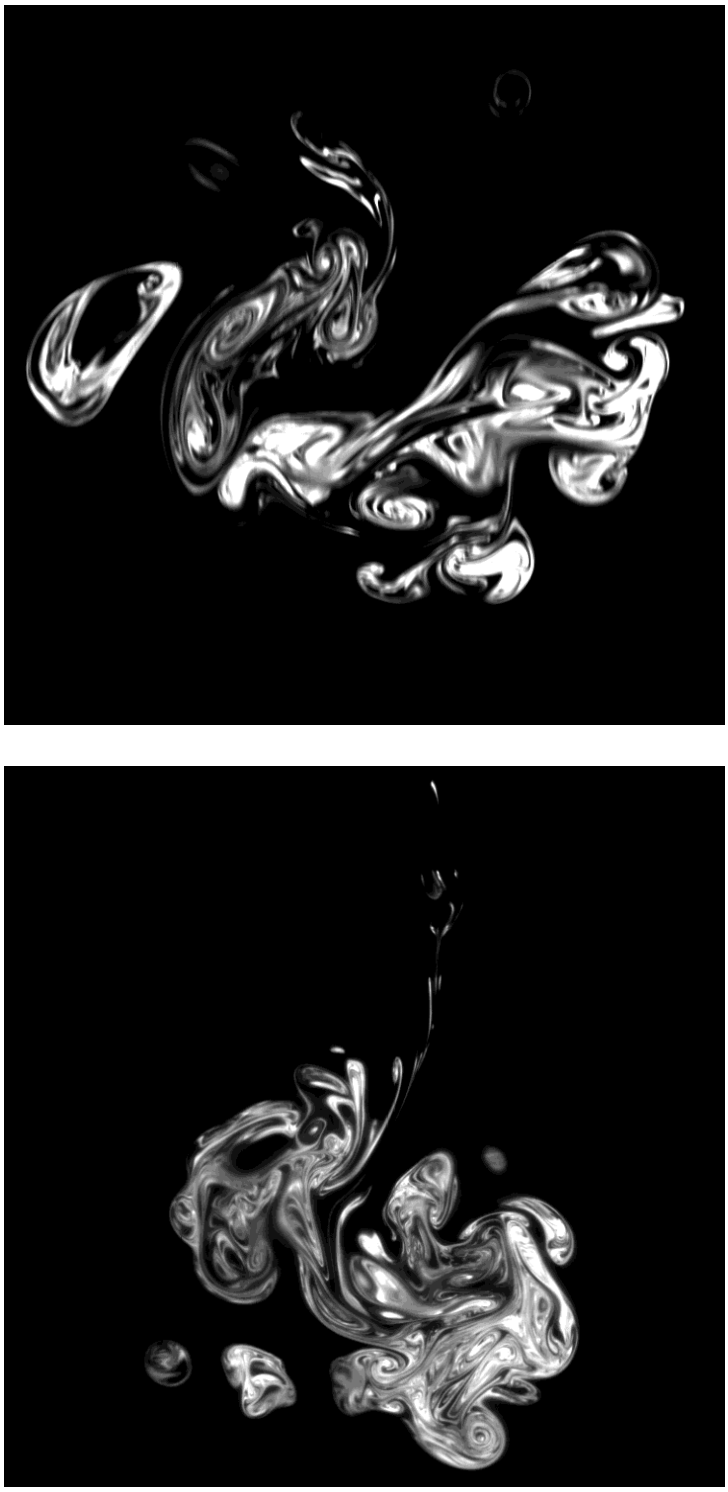

FIG. 7 Jet-fluid concentration in a transverse slice of the jet for $Re_{\rm j} = 1.0 \times 10^3$. Top: $V_{\rm r} \simeq 10$ and $x/d_{\rm j} = 50$. Bottom: $V_{\rm r} \simeq 32$.

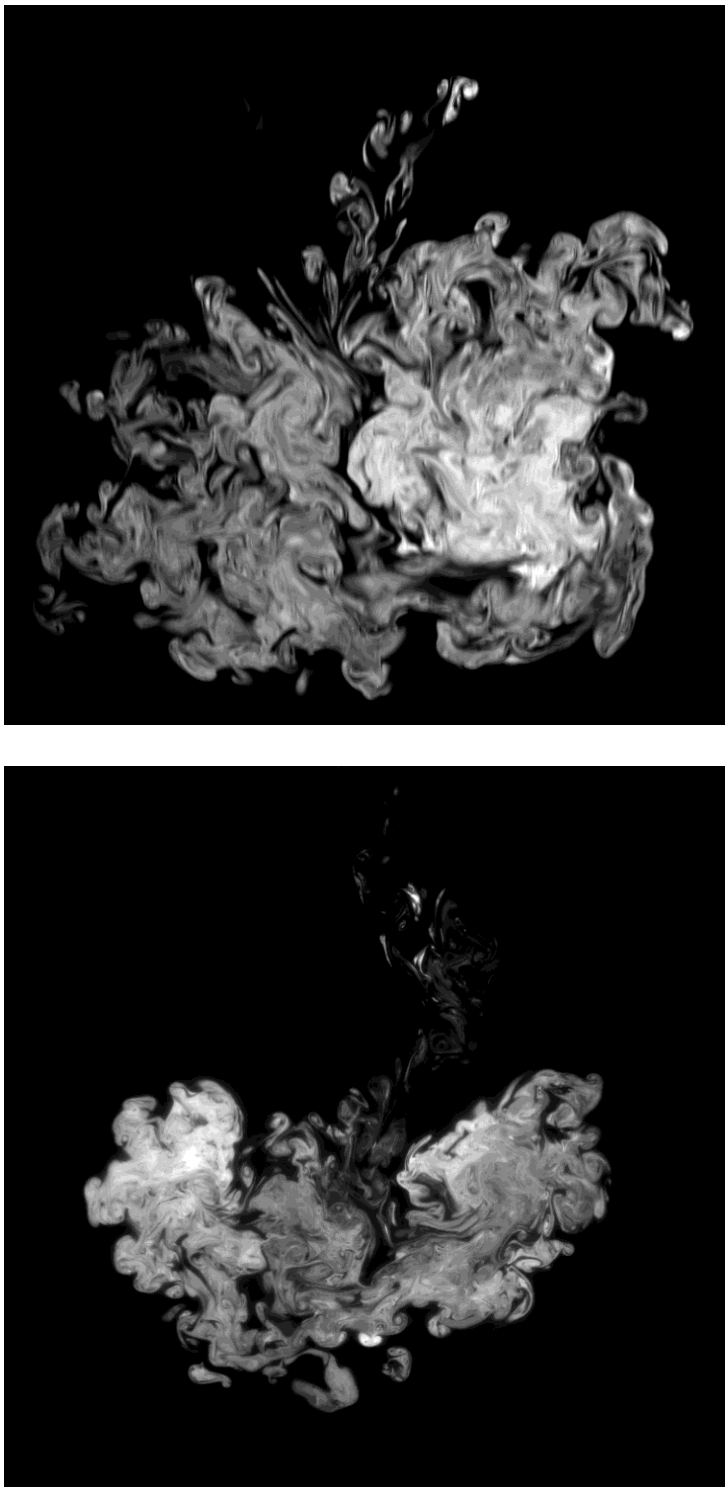

FIG. 8 Jet-fluid concentration in a transverse slice of the jet for $Re_{\mathrm{j}} = 10 \times 10^3$. Top: $V_{\mathrm{r}} \simeq 10$ and $x/d_{\mathrm{j}} = 50$. Bottom: $V_{\mathrm{r}} \simeq 32$.

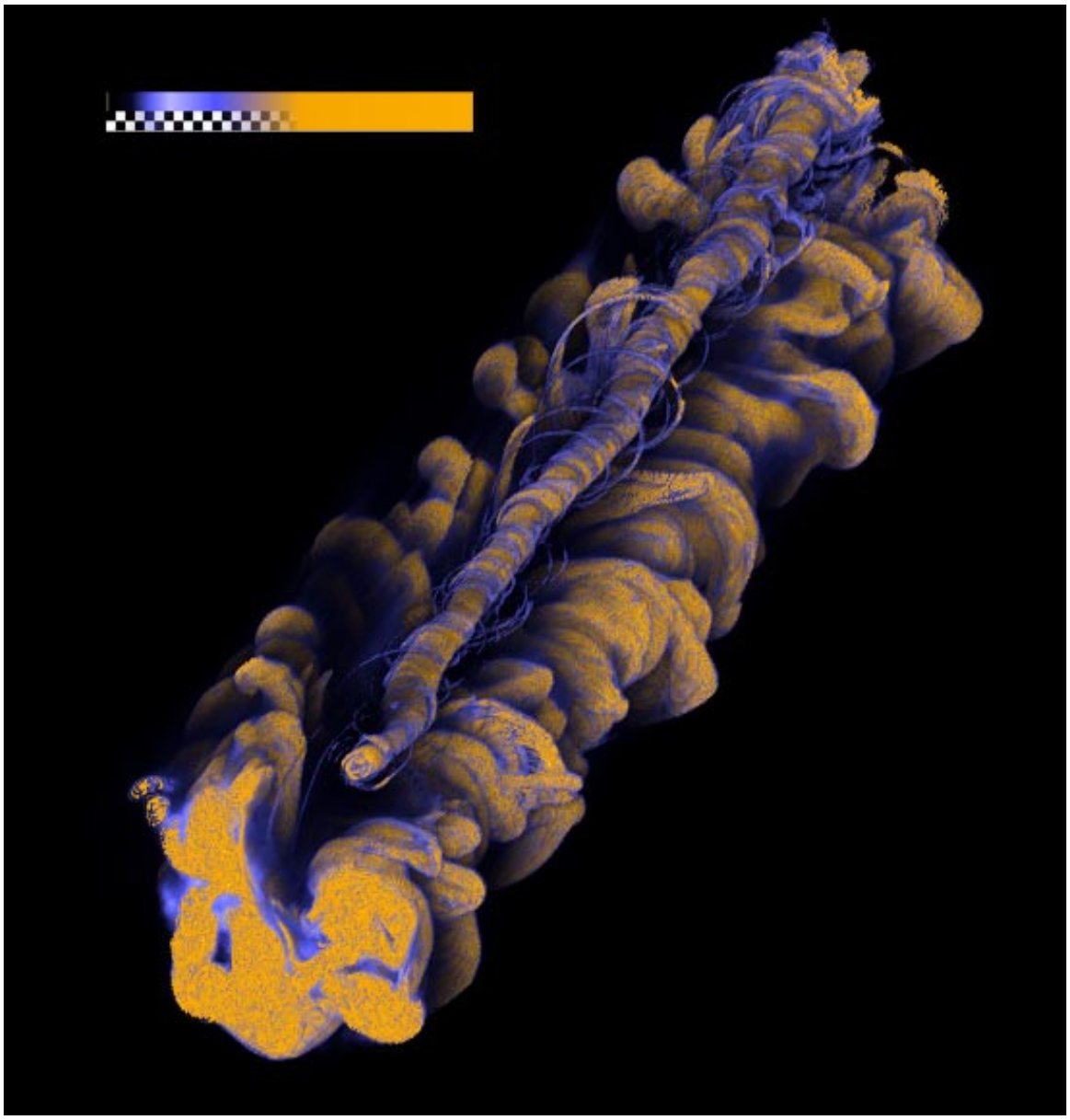

FIG. 9 Three-dimensional, space-time visualization of an isosurface of jet-fluid concentration for $Re_{\rm j} \simeq 1.0 \times 10^3$, $V_{\rm r} = 10.1$ transverse jet. Time runs along the axis of the vortices. The visualization was computed in collaboration with Santiago Lombeyda of Caltech's CACR.

Another space-time visualization, but for $Re_{\rm j} \simeq 2.0 \times 10^3$, is shown in Fig. 10. In comparison to the $Re_{\rm j} \simeq 1.0 \times 10^3$ case, the transverse-jet isosurface at $Re_{\rm j} \simeq 2.0 \times 10^3$ is roughly symmetric. Once again, the structure of the transverse jet is dominated by a kidney-shaped, counter-rotating vortex pair. Filaments are again seen to extend vertically from the main body of the jet. However, a tertiary vortex is not seen in the higher Reynolds number case.

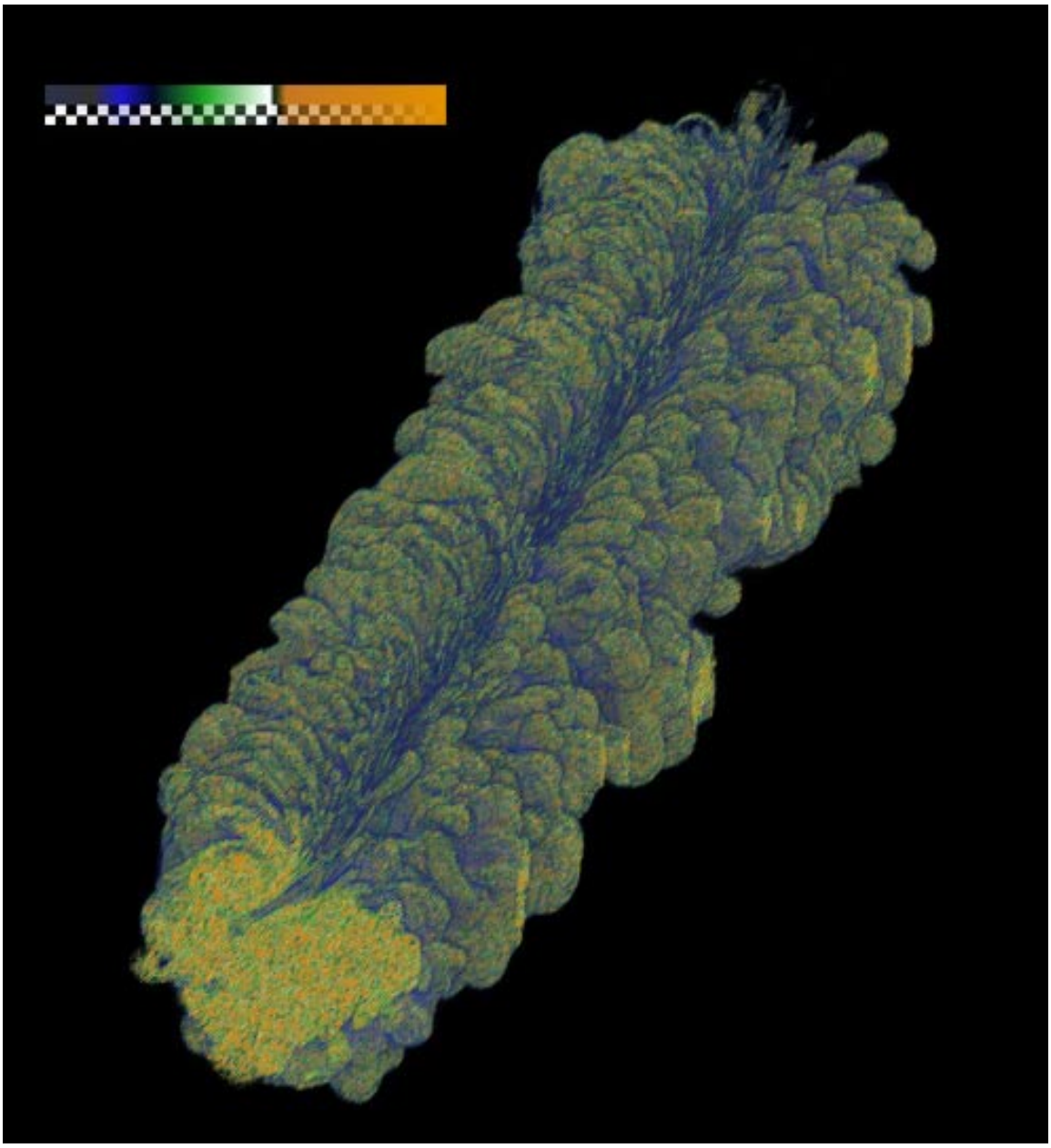

FIG. 10 Three-dimensional,space-time visualization of an isosurface for $Re_{\rm j} \simeq 2.0 \times 10^3$, $V_{\rm r} = 10.1$ transverse jet. The visualization was computed in collaboration with Santiago Lombeyda of Caltech's CACR.

These visualizations are consistent with the results of Kuzo (1996), who performed particle-image-velocimetry experiments to measure vorticity fields in transverse jets at comparable Reynolds numbers and velocity ratios. Kuzo found asymmetric flow states, and tertiary and quaternary vortices, in the transverse jet at low Reynolds numbers. However, we caution that direct comparison is not possible between measurements of the scalar field, and measurements of the vorticity field.

4. Local Reynolds number and dissipation scales

For an axisymmetric jet discharging into a quiescent reservoir, the local Reynolds number, $Re(x) \equiv \delta(x) U_{\rm m}/\nu$, is constant after several nozzle diameters, $d_{\rm j}$. Here, $\delta(x)$ is the local width of the jet, $U_{\rm m}$ is the local mean centerline velocity, and ν is the kinematic viscosity. The local Reynolds number in the case of the turbulent jet in a quiescent reservoir is approximately equal to the jet-exit Reynolds number, $Re_{\rm j} \equiv d_{\rm j} U_{\rm j}/\nu$, where $U_{\rm j}$ is the jet-exit velocity. However, as will be shown, the local Reynolds number for the transverse jet is not constant in the far field, but decays with increasing downstream distance.

We follow Broadwell and Breidenthal (1984) in considering a jet of density ρ_j and velocity $U_{\rm j}$ discharging perpendicularly into a freestream of density ρ_∞ and velocity U_∞. In the limit in which the jet momentum flux, $\dot{m}_{\rm j} U_{\rm j} = \rho_j \pi (d_{\rm j}/2)^2 U_{\rm j}^2$, is held constant as jet diameter, $d_{\rm j}$, decreases, and the discharge velocity, $U_{\rm j}$, increases accordingly, the jet approaches a point source of normal momentum. This source of normal momentum, a "lift" force of vanishing drag, generates a counter-rotating vortex pair that is the analogue of tip-vortices behind a lifting wing. Broadwell and Breidenthal argue from dimensional analysis that, if viscosity has no global role and only serves to dissipate energy at the Kolmogorov scale, then the only global length scale for this limiting case of the transverse jet is:

$$l \;=\; \left(\frac{\dot{m}_{\rm j} U_{\rm j}}{\rho_\infty U_\infty^2} \right)^{1/2} \;\propto\; V_{\rm r}\, d_{\rm j}\,, \tag{3}$$

for $V_{\rm r} \equiv U_{\rm j}/U_\infty$, and equal jet and free-stream densities, $\rho_j = \rho_\infty$. The circulation of one vortex, Γ, the vortex-core separation distance, R, and the vortices' vertical velocity, $\mathrm{d}y/\mathrm{d}t$, are related by

$$\frac{\mathrm{d}y}{\mathrm{d}t} \;=\; \frac{c_1 \Gamma}{R}\,. \tag{4}$$

The fluid impulse per unit length, P, is related to the circulation, Γ, and the vortex-core separation by

$$P \;=\; c_2\, \rho_\infty \Gamma R\,. \tag{5}$$

The value of the constants c_1 and c_2 in the two proceeding equations depend on the distribution of vorticity in the vortex pair, *e.g.*, for line vortices, $c_1 = \pi/4$ and $c_2 = 2$. Equations 4 and 5 assume that the transverse jet forms a single counter-rotating vortex pair, in the far field. As noted in Sec. 3, tertiary and quaternary vortices are sometimes formed, particularly at low Reynolds numbers. In such a situation, the vortices would no longer have equal circulation, and each vortex could

have a different induced velocity. The induced downward velocities, $\mathrm{d}y/\mathrm{d}t$, would be substantially smaller, and the overall mean trajectory of the jet, $y(x)$, would be shallower. For simplicity, we consider the high Reynolds-number case, in which a single vortex pair is always found. Assuming a similarity form in which the flow is independent of l in the far field (*i.e.*, R is proportional to y), Eq. 5 may be substituted into Eq. 4, and integrated to find

$$y = c_3 \left(\frac{P}{\rho_\infty}\right)^{1/3} t^{1/3} . \tag{6}$$

We use the (far-field) transformation $x = U_\infty t$, and note that $P = \dot{m}_\mathrm{j} U_\mathrm{j}/U_\infty$, to find that the trajectory is (Broadwell and Breidenthal 1984)

$$\frac{y}{l} = c_3 \left(\frac{x}{l}\right)^{1/3} .$$

The circulation of one vortex is

$$\frac{\Gamma}{U_\infty l} \;=\; c \left(\frac{x}{l}\right)^{-1/3} , \tag{7}$$

where x is downstream (horizontal) distance from the jet exit, and c is a constant. This result may be expected to hold in the far field ($x \gg l$) of high-velocity ratio ($V_\mathrm{r} \gg 1$) transverse jets. Although the fluid impulse per unit length, P, is constant, the separation distance, R, is a function of x. Thus, the circulation is found to be a decreasing function of downstream distance, x. This is consistent with the physical picture of two counter-rotating vortices in close proximity decaying through viscous diffusion.

For high Reynolds-number transverse jets, the counter-rotating vortex pair is the dominant structure, and theprimary mechanism for entrainment of irrotational freestream fluid. In this case, a circulation-based Reynolds number, Re_Γ, is defined based on the vortex circulation,

$$Re_\Gamma(x) \equiv \frac{\Gamma}{\nu} \;=\; c\,\frac{U_\infty l}{\nu} \left(\frac{x}{l}\right)^{-1/3} . \tag{8}$$

This local, circulation-based, Reynolds number, $Re_\Gamma(x)$, is likely more relevant to turbulence and mixing in the transverse jet than the jet-exit Reynolds number, The local Reynolds number, $Re_\Gamma(x)$, is seen to be related to the jet-exit Reynolds number, Re_j, as

$$Re_\Gamma(x) \;=\; c\,\frac{U_\mathrm{j} d_\mathrm{j}}{\nu} \left(\frac{x}{l}\right)^{-1/3} \;=\; c\,Re_\mathrm{j} \left(\frac{x}{l}\right)^{-1/3} , \tag{9a}$$

where we have used $l = V_{\rm r}\, d_{\rm j}$. For a given velocity ratio, the local Reynolds number decays as $(x/d_{\rm j})^{-1/3}$ with increasing downstream distance. Although the precise value of the constant, c, is undetermined, we expect the local Reynolds number, $Re_\Gamma(x)$, to approach the jet-exit Reynolds number, $Re_{\rm j}$, as $x/l \to 1$. Taking the constant $c \simeq 1$, and using the conditions of the present experiments ($x/d_{\rm j} = 50$ and $V_{\rm r} = 10$), we find

$$Re_\Gamma(x) \;=\; Re_{\rm j} \left(\frac{x/d_{\rm j}}{V_{\rm r}} \right)^{-1/3} \;\simeq\; 0.6\, Re_{\rm j}. \tag{9b}$$

Thus, for $V_{\rm r} = 10$ jets, the jet-exit Reynolds number, $Re_{\rm j}$, is related to local, outer-scale, Reynolds numbers at $x/d_{\rm j} = 50$ by a factor of 0.6.

For sufficiently high Reynolds numbers, the Taylor-microscale Reynolds number, Re_λ, based on the root-mean-squared fluctuation of one component of velocity, $u_{\rm rms}$, and the Taylor microscale, λ, is related to the outer Reynolds number by (*e.g.*, Frisch 1995)

$$Re_\lambda \;\equiv\; \frac{u_{\rm rms}\lambda}{\nu} \;\simeq\; Re^{1/2}\,.$$

Taking Re to be the circulation-based Reynolds number, Re_Γ, we estimate that the highest Taylor Reynolds numbers reached in this experiment to be 110. The scalar-species equivalent of the Peclet number for this flow, $Re_\lambda Sc$, is estimated to be 920×10^3 for the highest-Reynolds-number case.

An estimate of the dissipation scales of the flow is made based upon the local Reynolds number, $Re_\Gamma(x)$. The Kolmogorov scale, based upon the energy dissipation rate, ϵ, is defined as

$$\lambda_{\rm K} \;\equiv\; \left(\frac{\nu^3}{\epsilon} \right)^{1/4}\,. \tag{10}$$

No estimate for the energy dissipation rate, ϵ, is available in the literature for transverse jets. Rather than a direct estimate from Eq. 10, a scaling argument is used to relate the Kolmogorov scale, $\lambda_{\rm K}$, to the (local) outer scale, $\delta(x)$, as

$$\frac{\lambda_{\rm K}}{\delta(x)} \;\simeq\; c_3 Re(x)^{-3/4}\,, \tag{11a}$$

where $Re(x)$ is the local Reynolds number. Here we take the local Reynolds number to be the circulation-based Reynolds number, *i.e.*, $Re(x) \equiv Re_\Gamma$. The constant, c_3, in Eq. 11 is taken to be unity on the basis of results in turbulent jets (Dimotakis 2000). For the experiments on the transverse jet described here, the outer scale $\delta(x)$ is of order 10^3 pixels. The Kolmogorov scale, based upon the local, circulation-based Reynolds number, is

$$\frac{\lambda_{\rm K}}{\delta(x)} \;\simeq\; Re(x)^{-3/4} \;\simeq\; Re_{\rm j}^{-3/4} \left(\frac{x}{l} \right)^{1/4}\,. \tag{11b}$$

Using Eq. 11, the Kolmogorov scales at $x/d_\mathrm{j} = 50$, referenced to the imaged pixel resolution, λ_p, are estimated to be $\lambda_\mathrm{K}/\lambda_\mathrm{p} \simeq 8.4,\ 5.0,\ 2.5,\ 1.5$, and 0.89, respectively, for jet Reynolds numbers $Re_\mathrm{j} = 1.0,\ 2.0,\ 5.0,\ 10$, and 20×10^3. The viscous scale, λ_ν, defined as the scale where the turbulence spectrum deviates from -5/3 power-law behavior, is estimated to be a factor of 50 times larger than the Kolmogorov scale, λ_K (Dimotakis 2000). This result is found to hold for a variety of flows across a wide range of Reynolds numbers.

The scalar diffusion scale, $\lambda_\mathcal{D}$, is estimated as a $Sc^{-1/2}$ multiple of the viscous scale, *i.e.*,

$$\lambda_\mathcal{D} \ \simeq \ Sc^{-1/2}\lambda_\nu = 50Sc^{-1/2}\lambda_\mathrm{K}\,, \tag{12}$$

where $Sc \equiv \nu/\mathcal{D}$ is the Schmidt number. For these experiments on liquid-phased transverse jets, at $V_\mathrm{r} = 10$ and $x/d_\mathrm{j} = 50$, the scalar diffusion scales are calculated to be $\lambda_\mathcal{D}/\lambda_\mathrm{p} \simeq 4.6,\ 2.7,\ 1.4,\ 0.82$, and 0.49, respectively, for jet Reynolds numbers $Re_\mathrm{j} = 1.0,\ 2.0,\ 5.0,\ 10$, and 20×10^3.

5. Trajectory, concentration decay, and power-spectra

An image of the mean-concentration field on the centerline of the transverse jet is shown in Fig. 11 for $Re_\mathrm{j} = 10 \times 10^3$. The mean-concentration image is ensemble-averaged from 254 individual measurements of the jet. Mean jet trajectories, defined as the locus of points of concentration maximum on the jet centerline, are also shown in Fig. 11 for for $Re_\mathrm{j} = 1.0$ and 10×10^3. Power-law trajectories of the form $y/d_\mathrm{j} \propto (x/d_\mathrm{j})^{0.28}$ were reported by Pratte and Baines (1967) in their experiments, while trajectories with exponent 1/3 were predicted by Broadwell and Breidenthal (1984). For comparison, lines of slope 1/4 and 1/3 are shown in Fig. 11. Experiments (*e.g.*, Kamotani & Greber 1972), as well as simulations (*e.g.*, Yuan *et al.* 1999), have shown that scalar-maxima trajectories are shallower than maximum-velocity or mean nozzle-streamline trajectories.

The concentration decay of the maximum mean concentration on the centerline of the transverse jet is plotted in Fig. 12 as a function of downstream distance, x/d_j, and penetration depth, y/d_j. Two Reynolds numbers are considered, $Re_\mathrm{j} = 1.0$ and 10×10^3. Decay with penetration depth is Reynolds-number dependent for the first 6 nozzle diameters, but then becomes independent with greater distance from the jet exit. The difference at the beginning is attributable to the longer laminar-jet

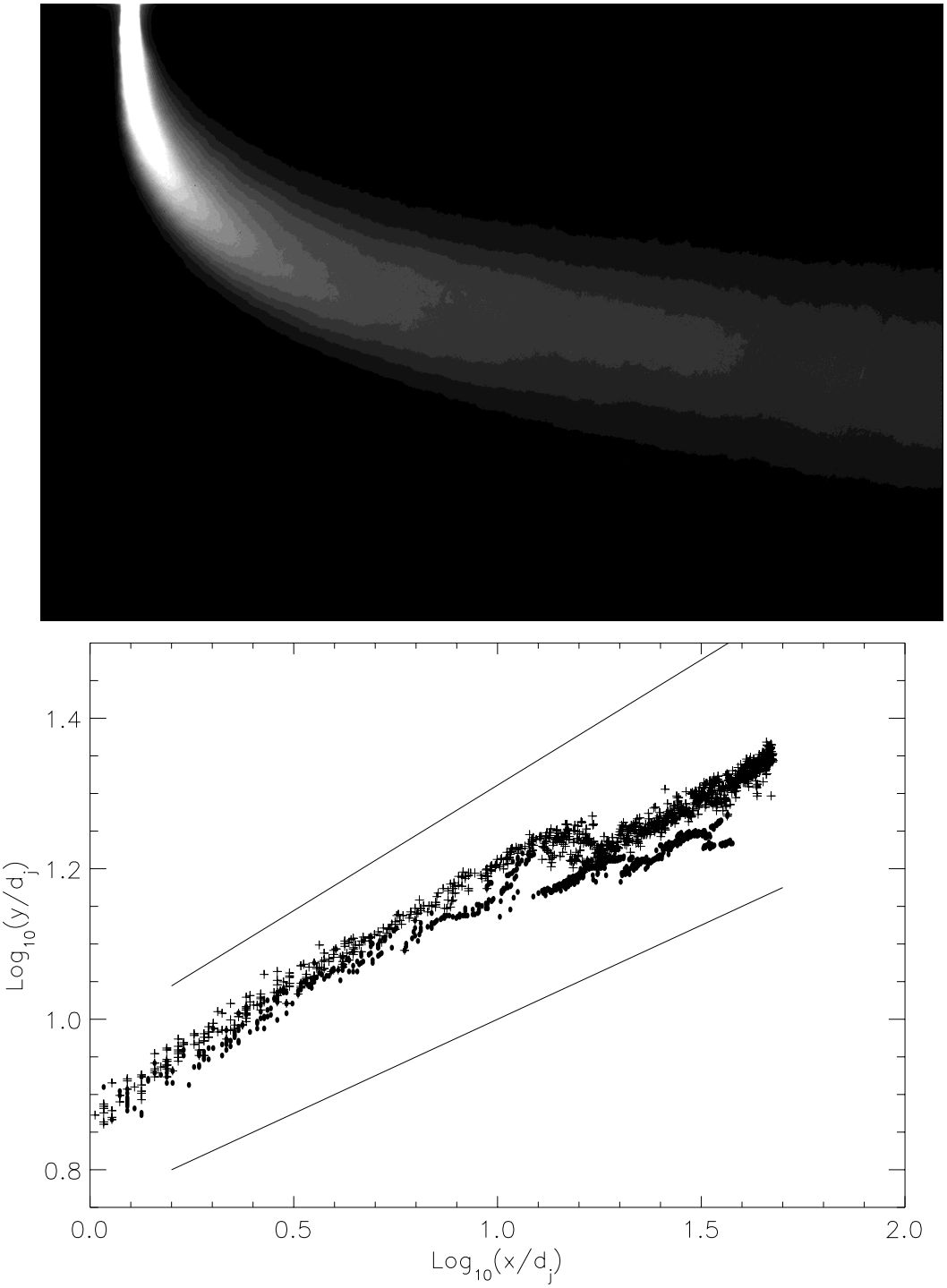

FIG. 11 Mean concentration field and jet-centerline trajectory. Left: Ensemble-averaged concentration field for $Re_{\rm j} = 10 \times 10^3$ and $V_{\rm r} \simeq 10.1$. Right: Maximum jet-fluid-concentration trajectory. Penetration depth versus downstream distance with logarithmic axes. Lower comparison line is $y/d_{\rm j} \propto (x/d_{\rm j})^{1/4}$ (*cf.* experiments of Pratte & Baines 1967). Upper comparison line is $y/d_{\rm j} \propto (x/d_{\rm j})^{1/3}$ (*cf.* prediction of Broadwell and Breidenthal 1984). Trajectories plotted with circles for $Re_{\rm j} = 1.0 \times 10^3$, with crosses for $Re_{\rm j} = 10 \times 10^3$.

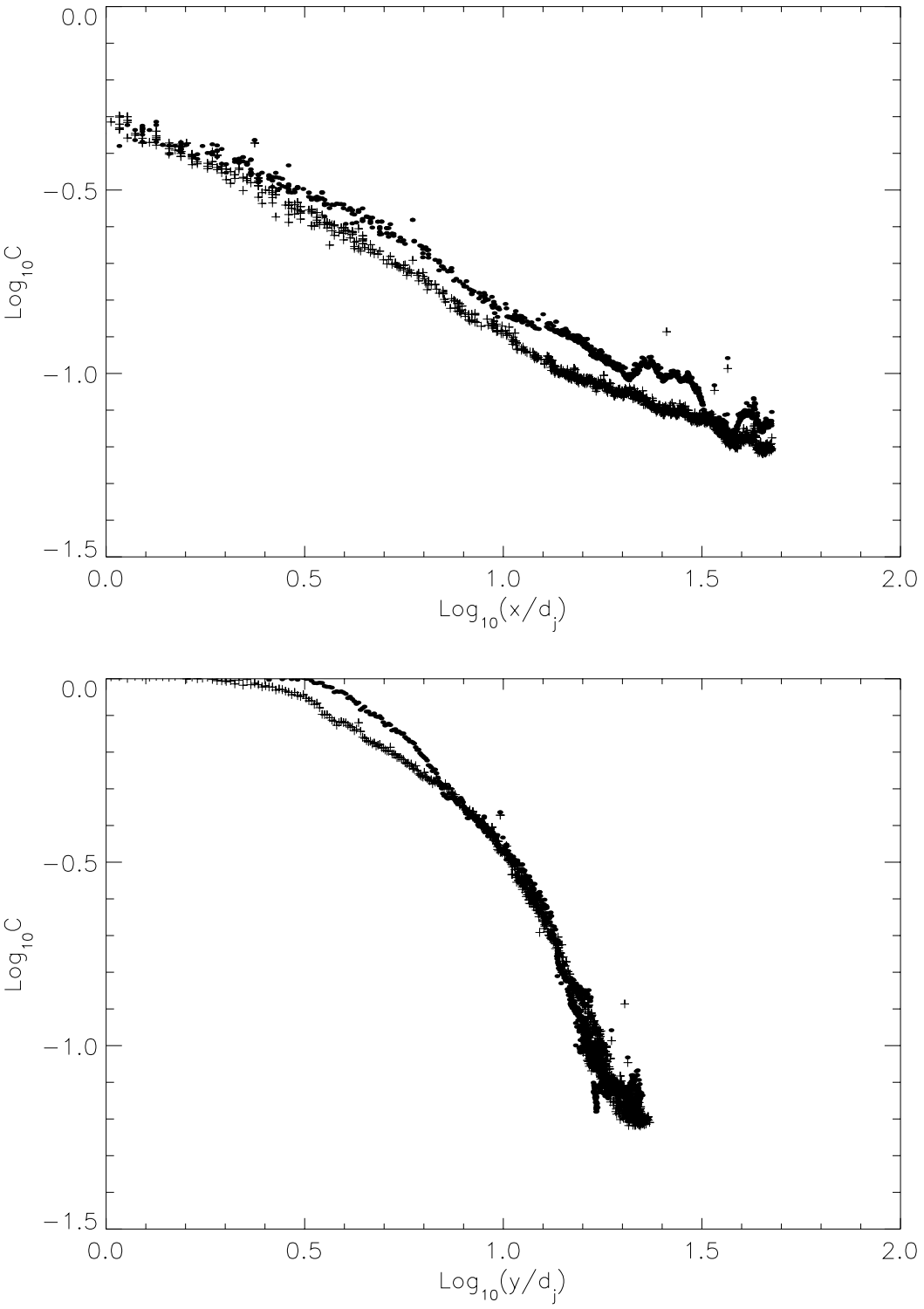

FIG. 12 Decay of maximum mean concentration, in logarithmic coordinates. $Re_{\rm j} = 1.0 \times 10^3$ is shown with circles, $Re_{\rm j} = 10 \times 10^3$ with crosses. Left: Concentration decay with downstream distance. Right: Concentration decay with penetration depth.

length for the lower-Reynolds-number case. For $y/d_{\rm j} \geq 6$, the initially slower-mixing, $Re_{\rm j} = 1.0 \times 10^3$, jet is unsteady and its decay trajectory overlaps with that of the $Re_{\rm j} = 10 \times 10^3$ jet.

The horizontal spatial extent, $\delta_{\rm h}$, of the scalar field, based on the mean scalar field at $x/d_{\rm j} = 50$, is depicted in Fig. 13. This "size", $\delta_{\rm h}$, was defined by the horizontal extent of an area for which $< C > \geq \ 0.03 < C >_{\rm max}$. As seen in Fig. 13, the spatial extent of the transverse-jet scalar field is only slightly dependent on threshold value, and largely independent of Reynolds number. Excluding the slight peak at $Re_{\rm j} = 5.0 \times 10^3$, the spatial extent at $x/d_{\rm j} = 50$, is approximately $\delta_{\rm h}/d_{\rm j} = 23$ for all Reynolds numbers. This is to be expected since the global length scale, l, is constant across all Reynolds numbers for the jets considered in these experiments (Eq. 3).

Figure 14 shows power spectra of one-dimensional transects of the scalar field at $x/d_{\rm j} = 50$. The concentration power spectra, S_C, are normalized by the scalar variance, and non-dimensionalized by the spatial extent, $\delta_{\rm h}$, of the jet, *i.e.*,

$$S_C \ \equiv \ \frac{S_C(k\delta_{\rm h})}{\delta_{\rm h} \left\langle C'^2 \right\rangle} \,, \tag{13a}$$

where

$$\left\langle C'^2 \right\rangle \ = \ \frac{2}{\delta_{\rm h}} \int_0^\infty S_C(k\delta_{\rm h}) \, {\rm d}(k\delta_{\rm h}) \,. \tag{13b}$$

The spectra are computed from transects of the scalar image data at $x/dj = 50$. Transects were first Hann-windowed by convolving with a normalized function of the form $1 - {\rm Cos}(2\pi {\rm x_i}/\delta_{\rm x_i})$, where δ_{x_i} is the length of the transect in the x_i direction. Spectra were computed for both horizontal and vertical transects, and ensemble-averaged over each image, and averaged again over the entire sequence of 508 images. The spectra for horizontal and vertical transects are seen to deviate from one another, beginning at modest wavenumbers. This difference increases with increasing wavenumber, with less (scalar) energy in the vertical transects than in the horizontal transects. The anisotropy of the scalar field, as seen in the one-dimensional power spectra, persists over a wide range of Reynolds numbers.

Two-dimensional power spectra for the scalar field of the transverse jet are shown in Fig. 15, for $Re_{\rm j} = 1.0$ and 10×10^3. These were calculated as the modulus squared of the discrete Fourier transform of the jet-fluid concentration field at $x/d_{\rm j} = 50$. For each case, the ensemble average of 508, Hann-windowed measurements was taken. The contours, which would be circular for a statistically-isotropic

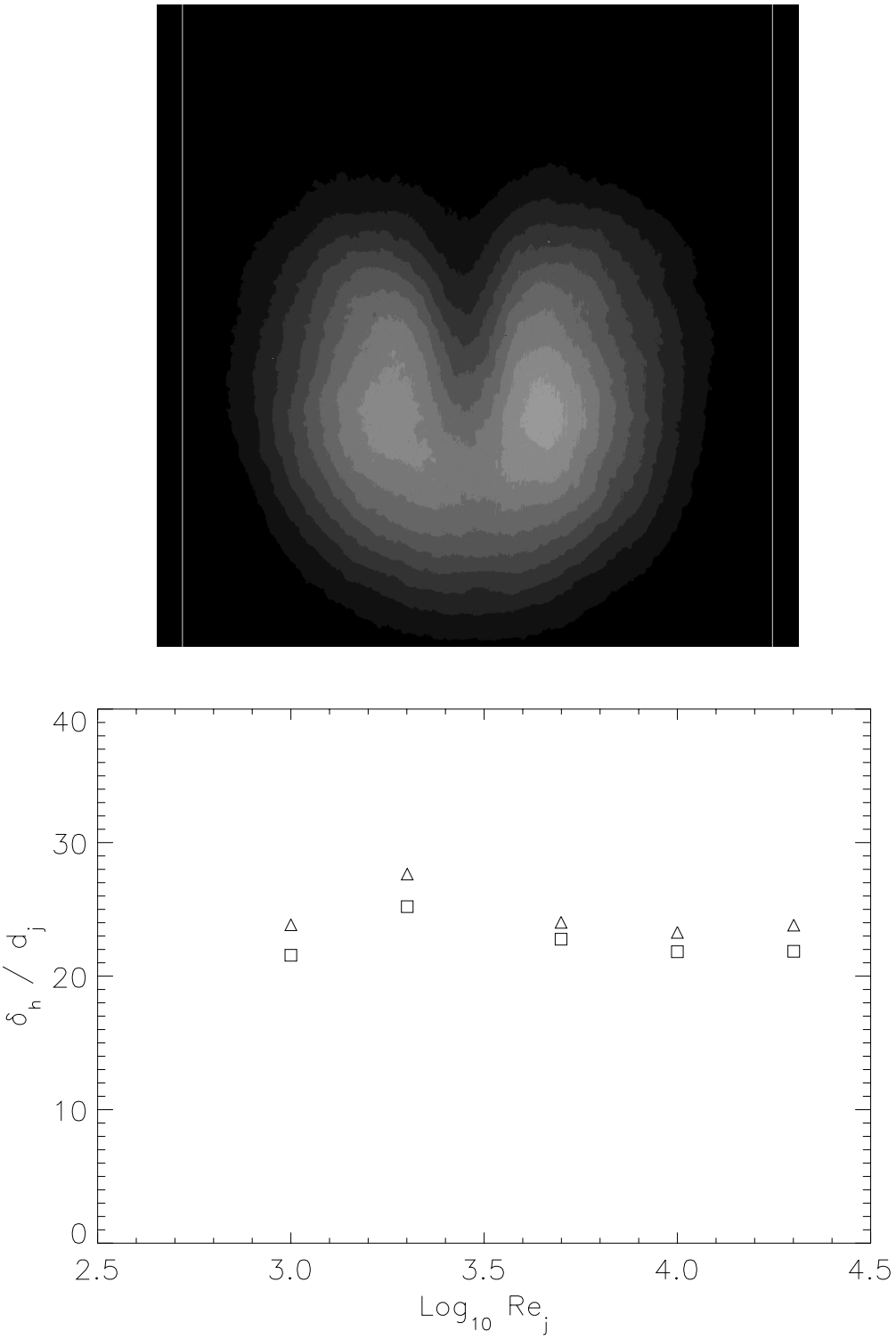

FIG. 13 Average spatial extent, δ_{h}, of scalar field at $x/d_{\mathrm{j}} = 50$. Top: Ensemble-averaged scalar field for $Re_{\mathrm{j}} = 20 \times 10^3$. Lines show horizontal extent for 3% of maximum mean concentration. Bottom: Spatial extent as a function of scalar threshold and Reynolds number. Triangles: 3% of maximum mean concentration. Squares: 5% of maximum mean concentration

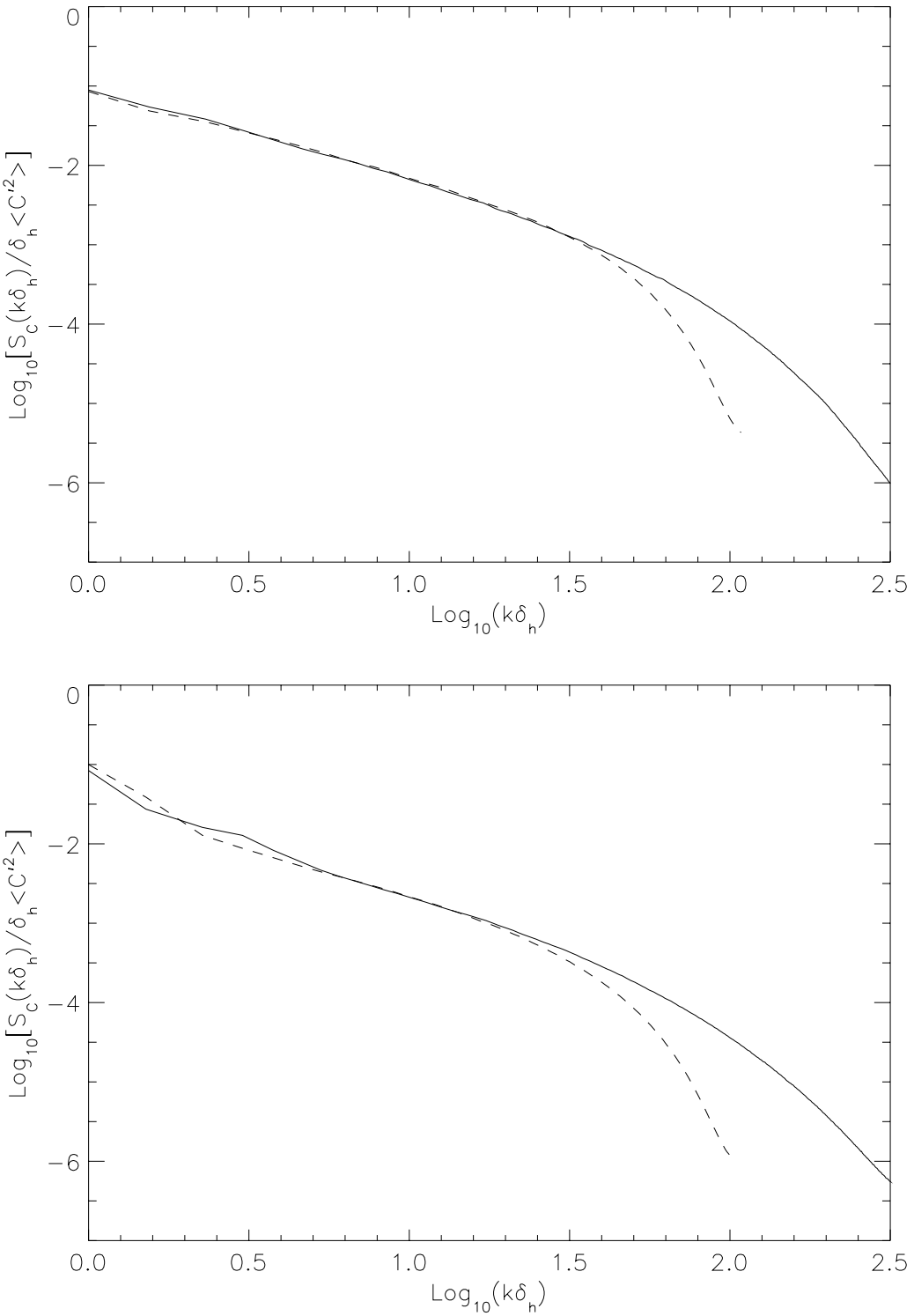

FIG. 14 Power spectra of one-dimensional transects of the scalar field at $x/d_{\rm j} = 50$. Solid line is for horizontal transects, and dashed line for vertical transects. Wavenumber, $\mathbf{k}$, normalized by spatial extent, $\delta_{\rm h}$. Top: $Re_{\rm j} = 1.0 \times 10^3$. Bottom: $Re_{\rm j} = 10 \times 10^3$.

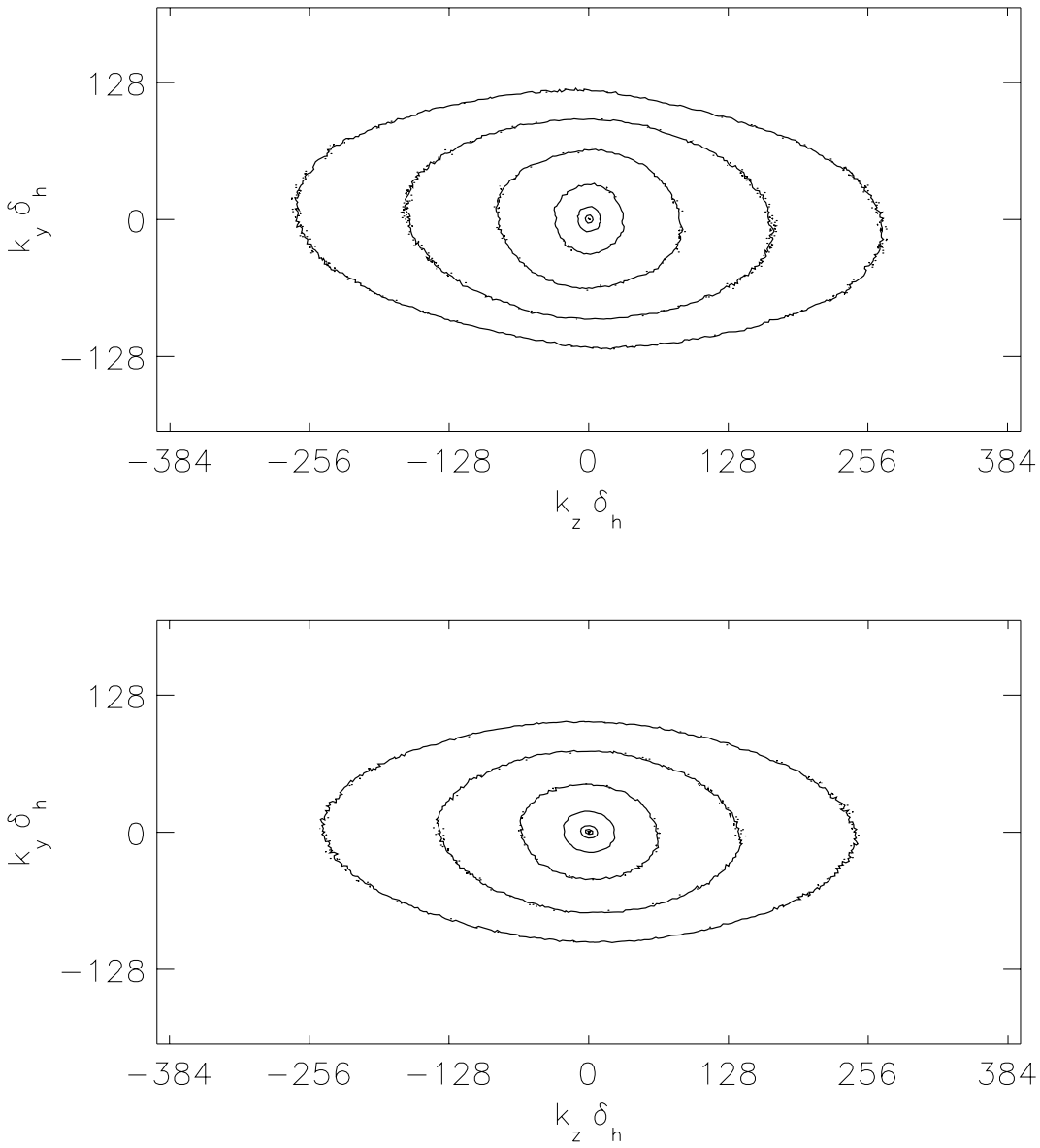

FIG. 15 Two-dimensional power spectra of the scalar field of the transverse jet at $x/d_\mathrm{j} = 50$. Wavenumber, $\mathbf{k}$, normalized by spatial extent, δ_h. Contour plot in $\log_{10}$ increments of 1. Top: $Re_\mathrm{j} = 1.0 \times 10^3$. Bottom: $Re_\mathrm{j} = 10 \times 10^3$.

field, are not axisymmetric, but increasingly elliptical with increasing wavenumbers. The orientation of the elliptical contours indicates that scalar gradients are steeper in the horizontal, rather than in the vertical, direction. At both Reynolds numbers, the small length scales, *i.e.*, higher wavenumbers, are more anisotropic than the large length scales. This observed anisotropy of the transverse jet's scalar field is in contrast to the far-field isotropy found for the axisymmetric jet discharging into a quiescent reservoir (*cf.* Catrakis & Dimotakis 1996).

6. Jet-fluid-concentration probability-density function

Probability-density functions (PDFs) describing the scalar field of the transverse jet are shown in Fig. 16. PDFs form the basis for many statistical approaches toward turbulent flow with chemical reaction, in which the Navier-Stokes equations, along the the scalar-transport and chemical-reaction equations, are recast into evolution equations for the joint distribution of flow variables (Pope 1985, Goldin & Menon 1997). They are defined such that their integrals give the probability that $C_1 \leq C < C_2$, *i.e.*,

$$\Pr\{C_1 \leq C < C_2\} = \int_{C_1}^{C_2} f(c)dc = F(C_1) - F(C_2)\,. \tag{14}$$

For the transverse jet, PDFs of jet-fluid concentration are computed from normalized histograms of the scalar image data. The PDFs, $f(C; Re)$, at each Reynolds number are estimated from 512 individual, (1024×1024)-pixel images, yielding 5.4×10^8 point measurements of the concentration field. Because of the large sample size, the distributions are well resolved in C.

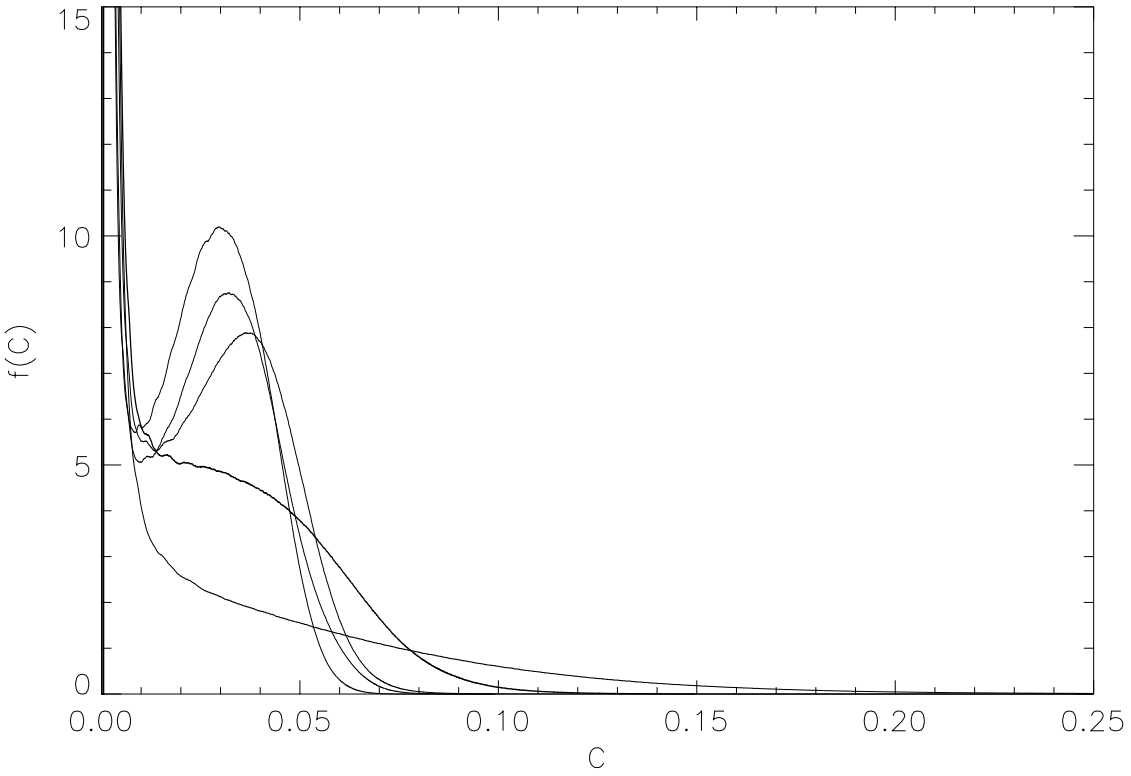

FIG. 16 Distributions of jet-fluid-concentration in transverse slices (*cf.* Fig. 7) of jet at $x/d_\mathrm{j} = 50$. Concentrations normalized by plenum-exit concentration, $C = c/c_0$. Increasingly peaked PDFs at $C \simeq 0.04$ with increasing Reynolds number for $Re_\mathrm{j} = 1.0$, 2.0, 5.0, 10, and 20×10^3.

Distributions described here are spatial, rather than temporal. That is, they are based on the probability of occurrence for C in a two-dimensional image, rather than on the frequency of occurrence at a fixed point in space. In particular, the spatial PDF is the normalized magnitude of the differential area associated with a differential concentration in two dimensions (Kuznetsov & Sabelnikov 1990, Dimotakis & Catrakis 1996),

$$f(C) \;=\; \frac{1}{A_{\rm tot}} \left| \frac{{\rm d}A(C)}{{\rm d}C} \right| , \tag{15a}$$

where $A(C)$ is the area associated with a specified value of the scalar concentration, and $A_{\rm tot}$ is the total area of the scalar field. In d-dimensions, the PDF is computed as,

$$f_n(C) \;=\; \frac{1}{V_{d,{\rm tot}}} \left| \frac{{\rm d}V_d(C)}{{\rm d}C} \right| , \tag{15b}$$

where $V_d(C)$ is the d-dimensional volume associated with C, and $V_{d,{\rm tot}}$ is the total, d-dimensional volume of the scalar field. The PDFs, in general, can depend not only on the statistics of the scalar field, but also on the dimensionality of the space or measurement (see Appendix).

Figure 16 shows PDFs for transverse slices of the jet at $x/d_{\rm j} = 50$, for Reynolds numbers $Re_{\rm j} = 1.0$, 2.0, 5.0, 10, and 20×10^3. The singularity in the distributions at the origin, $C = 0$, is a consequence of the unmixed, freestream fluid surrounding the spatially-confined jet. This singularity is excluded from the normalization of the PDFs. For the lowest Reynolds number, $Re_{\rm j} = 1.0 \times 10^3$, the distribution peaks around $C = 0$ and decreases monotonically with increasing scalar concentration. At double the Reynolds number, $Re_{\rm j} = 2.0 \times 10^3$, the PDF still decreases monotonically, but shows less probability for unmixed, high-C fluid. By Reynolds number 5.0×10^3, a distinct peak has formed in the distribution, near $C \simeq 0.04$. This peak grows with increasing Reynolds number, implying more-uniform mixing, *i.e.*, enhanced spatial homogenization, of the scalar field. The distribution of the scalar field, at fixed downstream location, qualitatively changes shape over the range $1.0 \times 10^3 \leq Re_{\rm j} \leq 20 \times 10^3$. Scalar mixing in the transverse jet is, in this sense, enhanced by increasing Reynolds number.

As an aside, we note that control-volume analysis shows that the mean concentration, $\bar{C}$, in a far-downstream transverse plane, depends linearly on the jet-exit concentration, c_0, and the velocity ratio, $V_{\rm r}$,

$$\bar{C} \;=\; \int_0^1 C\, f(C)\, {\rm d}C \;\simeq\; c_0\, V_{\rm r}\, \frac{A_{\rm j}}{A_{\rm tot}} \tag{16}$$

where A_j is the exit area of the nozzle and A_tot is the total area of the image plane. Recall that $0 \leq C \leq 1$, from Eq. 2. When c_0 and V_r are constant, as they were in these experiments, the mean concentration, $\bar{C}$, in a far-downstream plane should be independent of Reynolds number. This was verified in these measurements.

For comparison, PDFs of axisymmetric, turbulent jets discharging into a quiescent reservoir are shown in Fig. 17. These measurements, by Catrakis and Dimotakis (1996), were made in the far-field of liquid-phase jets for Reynolds numbers in the range $4.5 \times 10^3 \leq Re_\mathrm{j} \leq 18 \times 10^3$. For the turbulent jet discharging into a quiescent reservoir, the PDFs lost their peak at the highest Reynolds number. The "valley" on the low concentration side of the peak fills-in, and the preferred concentration, C_peak, shifts strongly toward lower concentrations. In contrast, distributions for the transverse jet have growing peaks with increasing Reynolds number. The flow-dependent mixing may be explained by noting that turbulent mixing is essentially a three-stage process (Eckart 1948, Dimotakis 1986): entrainment (engulfment of irrotational flow into the turbulent-flow region), stirring (kinematic motion responsible for creating interfacial area between species), and molecular mixing (diffusive mixing on the molecular scale). The balance between these three stages determines the mixed-fluid PDF. In particular, for the transverse jet, Smith and Mungal (1998) found the mean centerline concentration in the far field decayed as $s^{-2/3}$, where s is the distance along the jet trajectory. The mean concentration, which is calculated from ensemble averages of the scalar field, is unable to distinguish between distributions having the same first moment. Thus, it is a measure of entrainment, rather than molecular mixing. We infer, based on Smith and Mungal's experiments, that the transverse jet entrains less ambient fluid than the ordinary turbulent jet, which has a mean concentration decay proportional to s^{-1}. While it entrains less fluid for a given arclength, s, the transverse jet homogenizes the entrained fluid more thoroughly. The growing peaks in the scalar-field PDF for the transverse jet suggest that, in this case, the balance between entrainment, stirring, and molecular mixing tips in favor of stirring and molecular mixing. For ordinary jets, the entrainment rate is higher, and the balance tips toward entrainment. Flow-dependent mixing is possible, even for apparently similar turbulent flows, as a result of competition between entrainment, stirring, and molecular mixing. This is found to be the case for transverse jets, and jets discharging into a quiescent reservoir.

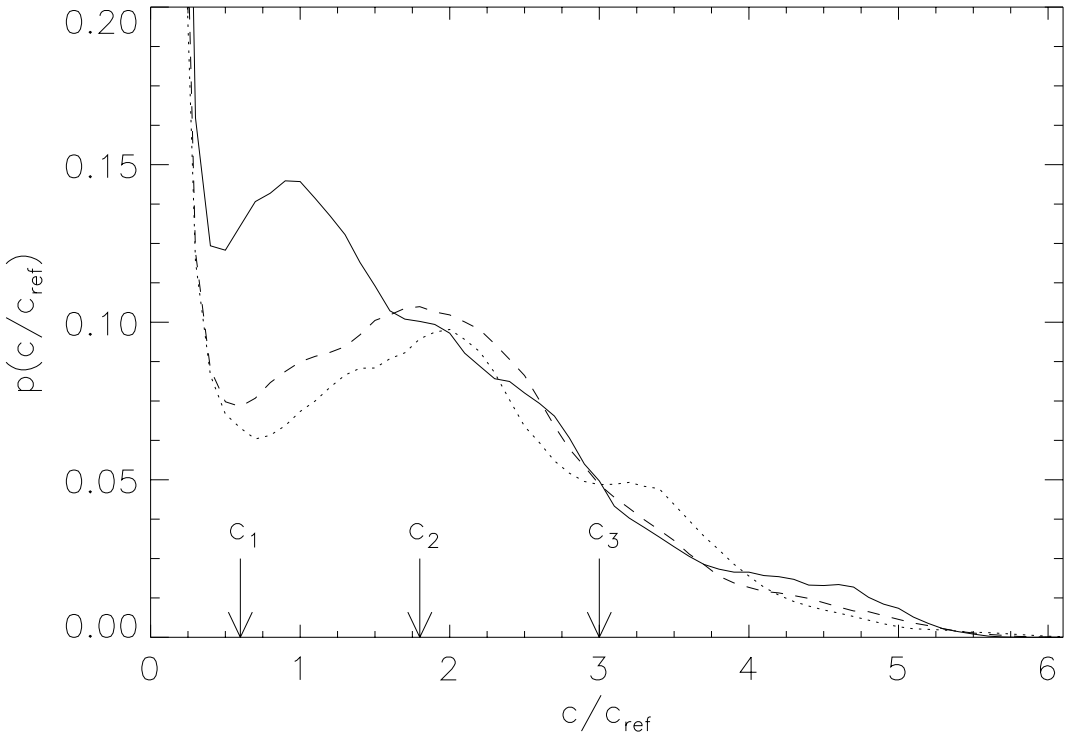

FIG. 17 Jet-fluid concentration PDFs for jets in a quiescent reservoir. Lines of increasing solidity denoting increasing $Re_{\rm j} = 4.5$, 9, and 18×10^3 (Catrakis and Dimotakis 1996, Fig. 8).

7. Probability-density function of scalar differences

The statistics of passive scalars and their derivatives in turbulence have been studied by numerous experimenters. Kailasnath *et al.* (1993) measured scalar concentrations (temperature and scalar-species concentration) and inferred scalar-dissipation rates, conditioned on scalar value, for turbulent wakes, jets, and boundary layers. Probability-density functions of temperature and temperature fluctuations were measured by Jayesh & Warhaft (1992), and Tong & Warhaft (1994), in grid turbulence, and by Alisse & Sidi (2000) in stably stratified atmospheres. Guilkey *et al.* (1997) reported on exponential-tailed scalar PDFs in turbulent-pipe-flow.

Much of our theoretical understanding of passive scalar fluctuations in turbulent flows is based upon the Richardson cascade (1922), and Kolmogorov's 1941 hypothesis. Oboukhov (1949) and Corrsin (1951) extended the notion of universality to scalars, to argue for a scalar cascade to small scales, where the scalar field would be locally isotropic (Warhaft 2000). One implication of the Kolmogorov-

Oboukhov-Corrsin (KOC) theory is a power-law scaling,

$$\langle [C(\mathbf{x}+\mathbf{r}) - C(\mathbf{x})]^n \rangle \;\sim\; r^{n/3} \tag{17}$$

for n^{th}-order scalar structure functions, $\langle [C(\mathbf{x}+\mathbf{r}) - C(\mathbf{x})]^n \rangle$. The n^{th}-order scalar structure functions for a turbulent flow maybe written as moments of the PDF of scalar increments, $\Delta_r C$, *i.e.*,

$$\langle [C(\mathbf{x}+\mathbf{r}) - C(\mathbf{x})]^n \rangle \;=\; \langle (\Delta_{\mathbf{r}} C)^n \rangle \;=\; \int_{-1}^{1} (\Delta_{\mathbf{r}} C)^n \, f(\Delta_{\mathbf{r}} C) \, \mathrm{d}\Delta_{\mathbf{r}} C \,, \tag{18}$$

where $0 \leq C \leq 1$. Thus, scalar differences, also called scalar increments, are important for developing models of turbulent mixing, and for testing the KOC theory and its refinements and extensions. Scalar increments are defined as the differences between simultaneous measurements of the scalar field at two points separated by vector distance $\mathbf{r}$, *i.e.*,

$$\Delta_{\mathbf{r}} C \;\equiv\; C(\mathbf{x}+\mathbf{r}, t) - C(\mathbf{x}, t) \,. \tag{19}$$

The PDF of scalar differences, $f(\Delta_{\mathbf{r}} C)$, expresses the probability of finding scalar concentration $C + \Delta C$ some distance $\mathbf{r}$ away from a point of concentration C.

The distribution of scalar differences is affected by internal intermittency of a turbulent scalar field. In particular, intermittency has been described as an excess of large fluctuations, compared to a Gaussian distribution of scalar differences (*e.g.*, Shraiman & Siggia 2000). The anomalous scaling (*i.e.*, departures from linearity in n) of the exponents for r in the structure functions defined in Eq. 17 is one consequence of internal intermittency. Anisotropy of the scalar field also manifests itself in the odd moments of the PDF of scalar differences, in the limit of high Reynolds numbers (Tong & Warhaft 1994, Warhaft 2000). For these reasons, data on the statistics of scalar increments is important for the theory and modelling of turbulent mixing flows . Much of the available data, however, is for temporal increments. The scalar difference data described in this paper are spatial increments, and do not make use of Taylor's hypothesis.

Statistics of temperature increments have been gathered by point measurements in a variety of flows, at low Prandtl numbers. Mydlarski & Warhaft (1998) measured spatial temperature differences in decaying grid turbulence. Ould-Rouis *et al.* (1995) reported on temporal temperature increments in a turbulent boundary layer. Antonia *et al.* (1984) conducted experiments on temperature differences on

the centerline of a turbulent plane jet, and found, for this flow, reasonable agreement between the statistics of temporal and spatial temperature increments. Ching (1991) reported on the PDFs of temporal temperature differences for Rayleigh-Benard convection at the center of a helium-gas cell. Collectively, these experiments found that PDFs of passive-scalar differences behaved like an exponential, or stretched exponential, at separations on the order of the Kolmogorov scale $r \sim \lambda_{\mathrm{K}}$, and tended toward Gaussian distributions for large, integral-scale separations $r \sim L$. A review of passive-scalar turbulence is given by Shraiman & Siggia (2000).

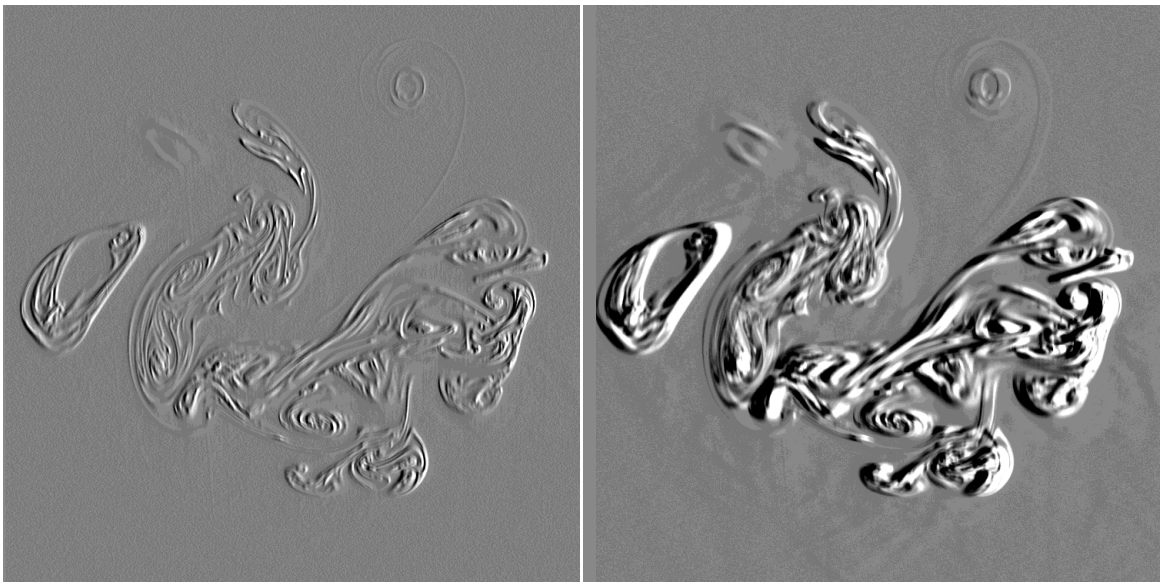

FIG. 18 Scalar-difference field for $Re_{\mathrm{j}} = 1.0 \times 10^3$. Left: Horizontal shift of $2.5 \times 10^{-3}\delta_{\mathrm{h}}$. Right: Horizontal shift of $21 \times 10^{-3}\delta_{\mathrm{h}}$. Grey denotes $\Delta_r C = 0$, and lighter/darker shades denote positive/negative values.

Two-dimensional image data of the type recorded in these experiments, enable whole-field, rather than point, measurements of spatial scalar increments. To compute scalar differences, measured concentration fields are spatially displaced by a vector distance $\mathbf{r}$, and subtracted from untranslated data. Examples of two-dimensional, scalar-difference fields are shown in Fig. 18, for horizontal displacements of $\mathbf{r}/\delta_{\mathrm{h}} = 2.5 \times 10^{-3}\,\widehat{\mathbf{z}}$ and $\mathbf{r}/\delta_{\mathrm{h}} = 21 \times 10^{-3}\,\widehat{\mathbf{z}}$. The distribution of scalar increments is computed from normalized, conditional histograms of such scalar-difference images. The histograms of $\Delta_{\mathbf{r}} C$ are conditioned on the intersection between shifted- and unshifted-image data, where the extent of the jet is defined by a scalar threshold. This is conceptually equivalent to requiring two instantaneous, spatially-separated measurements to both be within the body of the jet. The condition prevents the PDF from being dominated by the difference between the jet

and the freestream fluid. Without such a condition, the distribution of scalar increments would tend toward the concentration PDF, $f(C)$, and its reflection about the vertical axis, $f(-C)$, in the limit of large separations. The condition on the PDF is necessary because of the inhomogeneity, and spatial confinement, of the scalar field of the transverse jet.

Figure 19 shows conditional PDFs of scalar increments for varying horizontal separations. The PDFs were computed from measured jet-fluid-concentration fields at $x/d_\mathrm{j} = 50$, for $Re_\mathrm{j} = 2.0$ and 20×10^3. For the high Reynolds number case, $Re_\mathrm{j} = 20 \times 10^3$, the PDFs are exponential-tailed for small separation distances. In particular, the PDF of scalar increments has substantial exponential tails for $\mathbf{r}/\delta_\mathrm{h} \leq 2.5 \times 10^{-3}\,\widehat{\mathbf{z}}$. As separations become much larger than the viscous and scalar-diffusion scales, the shoulders of the PDFs broaden, and the tails drop. Ching (1991), for instance, has reported Gaussian PDFs of scalar increments for large separation distances. Decreasing probability for fluid of similar concentration, *i.e.*, decreasing $f(\Delta_\mathbf{r} C = 0)$, is seen with increasing separations. At low Reynolds numbers, $Re_\mathrm{j} = 2.0 \times 10^3$, the tails of the PDFs for small separations are no longer exponential, but rather stretched exponential. The shoulders of the PDF once again broaden with increasing separation distance.

The PDF of normalized scalar increments, $f(\Delta_\mathbf{r} C/\langle(\Delta_\mathbf{r} C)^2\rangle^{1/2})$, is shown in Fig. 20. These distributions are essentially the PDFs of Fig. 19, with the separation distance, r, has been normalized by the standard deviation of the scalar difference, $\langle(\Delta_\mathbf{r} C)^2\rangle^{1/2}$. For the range of Reynolds numbers studied, $2.0\times10^3 \leq Re_\mathrm{j} \leq 20\times10^3$, the normalized PDFs are found to have longer, exponential tails with decreasing separation distance. This excess of large concentration differences, relative to a Gaussian distribution, is one of the hallmarks of intermittency of the scalar field. The spike near the origin is also indicative of intermittency (Sreenivasan & Antonia 1997).

Anisotropy of the scalar field, particularly at small length scales, can be seen in PDFs of scalar increments for separations in different directions. Figure 21 compares scalar-difference fields for a horizontal shift of $\mathbf{r} = 2\widehat{\mathbf{z}}$ pixels and a vertical shift of $\mathbf{r} = 2\widehat{\mathbf{y}}$ pixels ($0.0022\delta_\mathrm{h}$). Both images use the same (linear) intensity scaling for scalar concentration. The occurrence of large scalar differences, shown as purely black or white features in the scalar-increment field, is more prominent for the horizontal separations than for the vertical ones, as also evident in the PDF statistics discussed below. This difference in contrast indicates that scalar structure is preferentially oriented in the vertical (y-axis) direction, and that scalar gradients

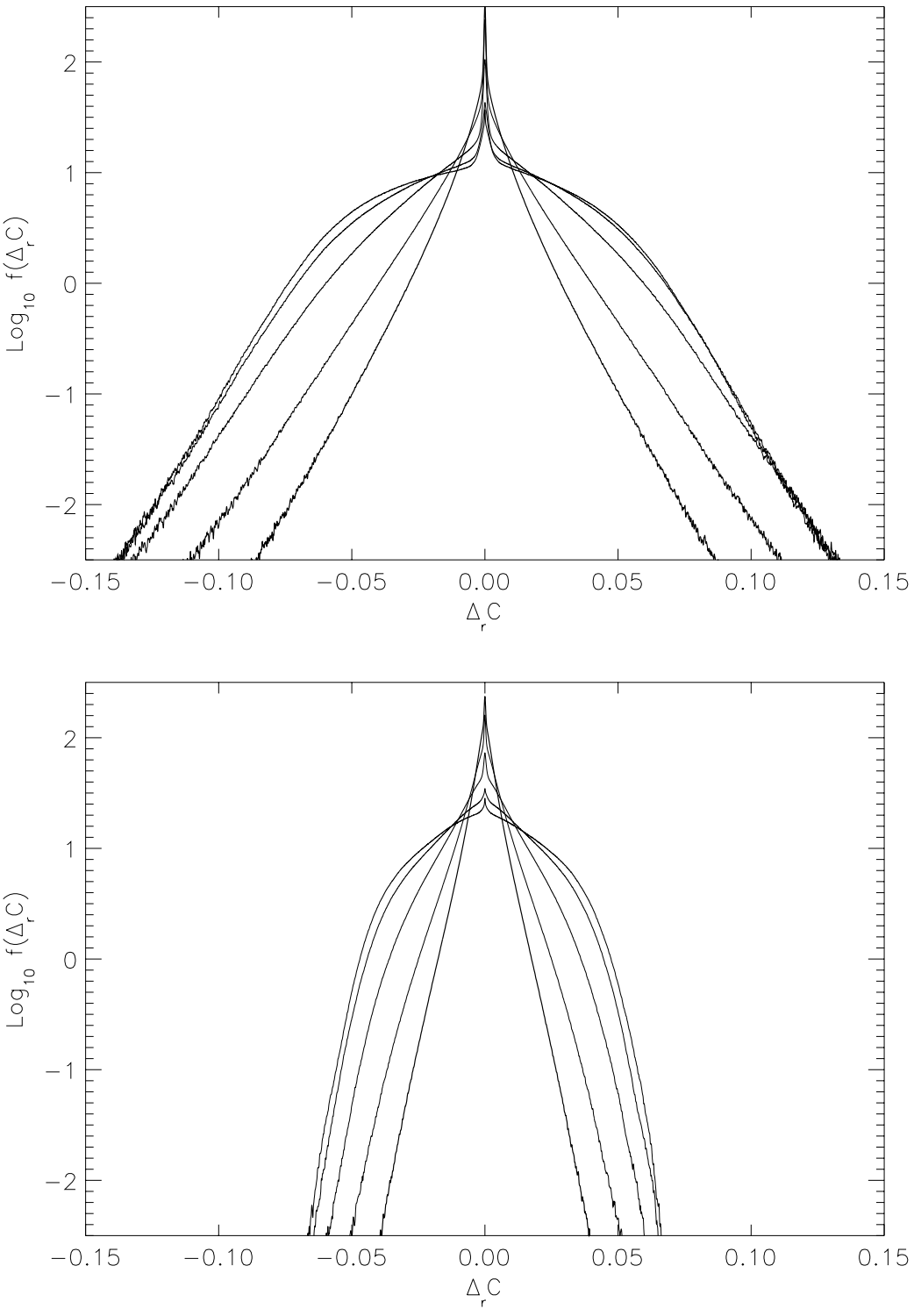

FIG. 19 Scalar-increment PDFs for varying separations. Innermost, triangular PDFs are for smallest separation distances, while outermost, broad-shouldered PDFs are for largest separations. Top: $Re_{\rm j} = 2.0 \times 10^3$ jet at $x/d_{\rm j} = 50$. Separation distances $\mathbf{r}/\delta_{\rm h} = 2.2$, 4.4, 17, 70, and $139 \times 10^{-3}\,\widehat{\mathbf{z}}$. Bottom: $Re_{\rm j} = 20 \times 10^3$. Separation distances $\mathbf{r}/\delta_{\rm h} = 2.5$, 5.1, 20, 81, and $162 \times 10^{-3}\,\widehat{\mathbf{z}}$.

CaltechGalcitFM:2001.006

are larger horizontally than vertically. Small-scale anisotropy of the scalar field is particularly apparent near the vertical centerline, and in the "finger" extending upwards at the top of the jet. The location of these small, vertically-oriented structures suggest that they are produced by the mean strain field of the dominant, counter-rotating vortex pair. Further evidence of this is described in Sec. 9.

Figure 22 shows distributions of scalar increments for horizontal and vertical separations of $2.2\times10^{-3}\delta_{\rm h}$ and $17\times10^{-3}\delta_{\rm h}$, at $Re_{\rm j}=2.0\times10^3$. For a distance of $17\times10^{-3}\delta_{\rm h}$, the PDFs for horizontal and vertical separations are essentially identical. For the smaller separation distance, $2.2\times10^{-3}\delta_{\rm h}$, the PDFs are narrower for vertical than for horizontal separations. This is an indication that, at small length scales, the scalar field has less variation along the vertical than in the horizontal direction, *i.e.*, more vertically-aligned structure. The anisotropy at small length scales persists throughout the Reynolds number range, $2.0\times10^3 \le Re_{\rm j} \le 20\times10^3$ (Fig. 23). This is consistent with the two-dimensional scalar power spectra, that were increasingly elliptical at higher wavenumbers, over a similar range of Reynolds numbers.

8. Scalar microscale

A microscale for fluctuations of the scalar field may be defined analogously to the Taylor microscale for velocity fields. For an isotropic scalar field, the scalar microscale, λ_C, is defined as (Tennekes & Lumley 1972):

$$\lambda_C^2 \equiv \frac{\left\langle C'^2 \right\rangle}{\left\langle \left(\frac{\partial C'}{\partial x}\right)^2 \right\rangle} \,. \tag{20a}$$

For an anisotropic field, the scalar microscale may be generalized to be directional, *i.e.*, (Cook & Dimotakis 2001),

$$\lambda_{C,i}^2 \equiv \frac{\left\langle C'^2 \right\rangle}{\left\langle \left(\frac{\partial C'}{\partial x_i}\right)^2 \right\rangle} \,, \tag{20b}$$

where $\lambda_{C,i}$ refers to the scalar microscale in a given direction, x_i.

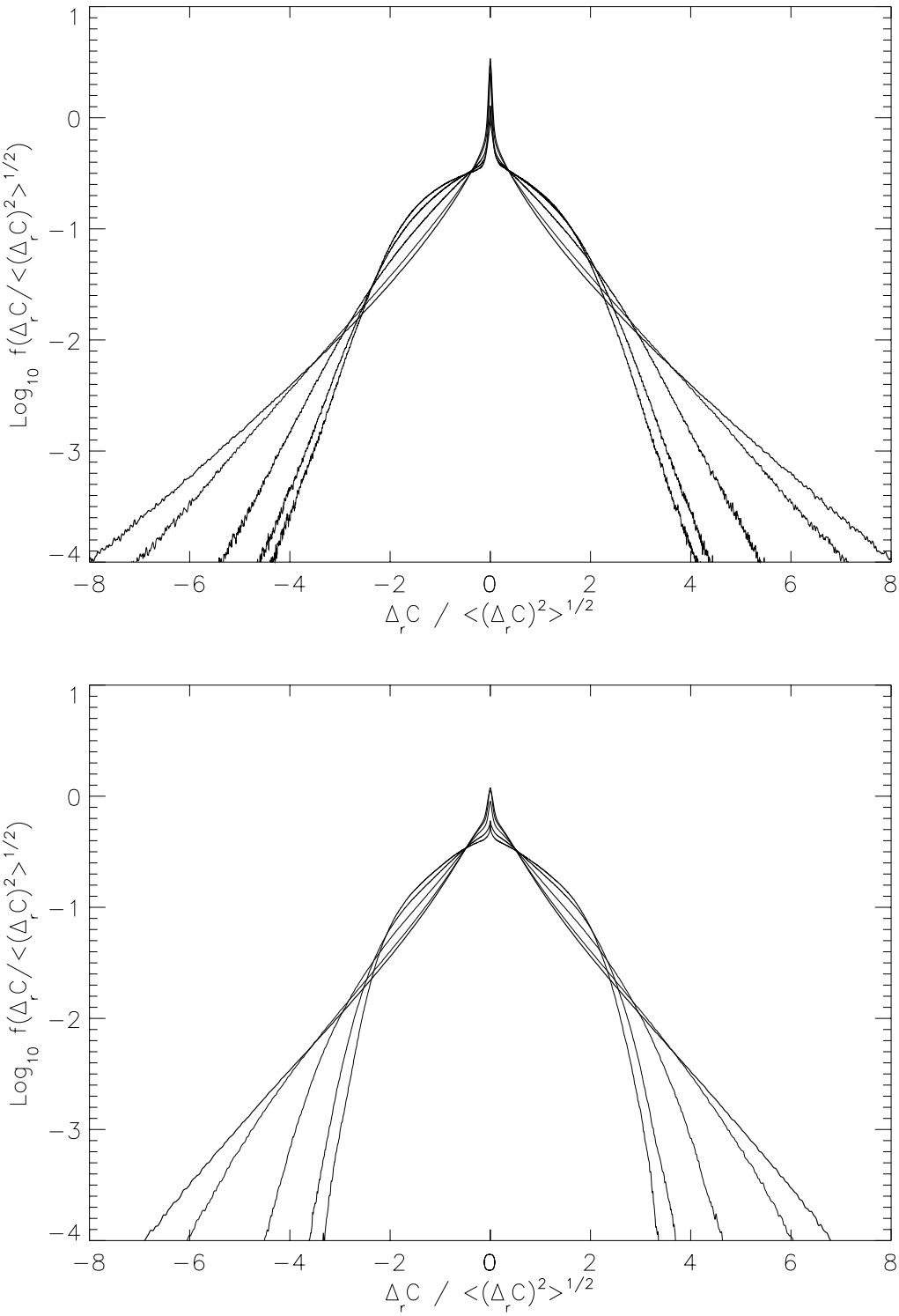

FIG. 20 PDFs of standard-deviation-normalized scalar increments for varying separations. Concentration difference is normalized by standard deviation for each distribution. Outermost, triangular PDF is for smallest separation distance, while innermost PDF is for largest separation. Top: $Re_{\rm j} = 2.0 \times 10^3$. Separation distances $\mathbf{r}/\delta_{\rm h} = 2.2$, 4.4, 17, 70, and $139 \times 10^{-3}\,\widehat{\mathbf{z}}$. Bottom: $Re_{\rm j} = 20 \times 10^3$. Separation distances $\mathbf{r}/\delta_{\rm h} = 2.5$, 5.1, 20, 81, and $162 \times 10^{-3}\,\widehat{\mathbf{z}}$.

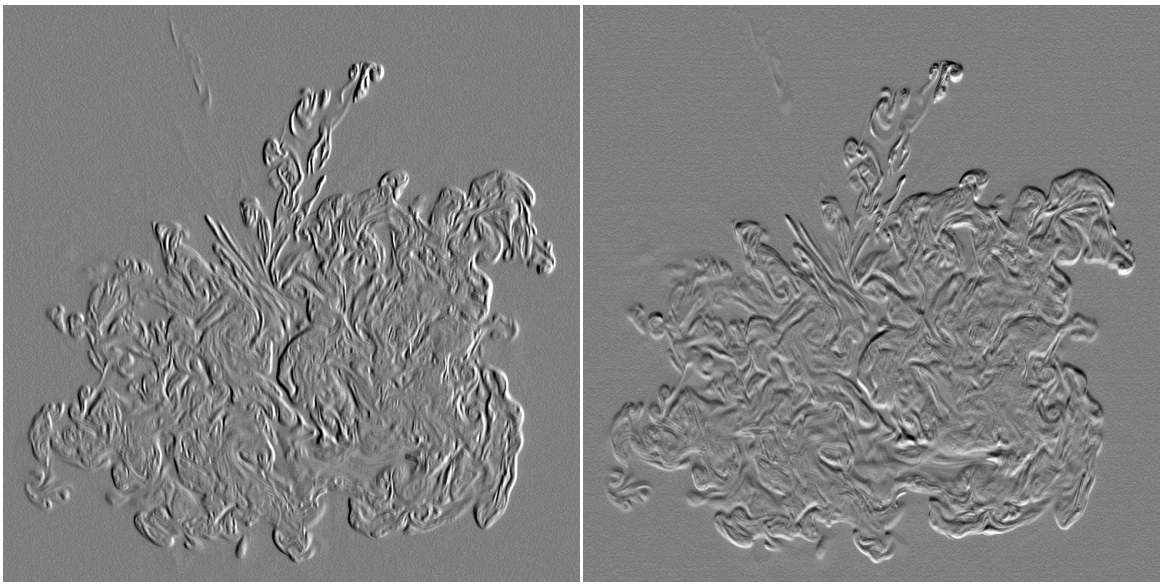

FIG. 21 Scalar difference field, $\Delta_{\mathbf{r}}C$, for different directions. Left: Horizontal shift of $\mathbf{r} = 2\,\widehat{\mathbf{z}}$ pixels for $Re_{\rm j} = 10 \times 10^3$. Right: Vertical shift of $\mathbf{r} = 2\,\widehat{\mathbf{y}}$ pixels. Same intensity scaling used both images.

Figure 24 shows the scalar microscales for $Re_{\rm j} = 1.0$, 2.0, 5.0, 10, and 20×10^3. The mean microscales at each Reynolds number are found by computing two orthogonal microscales for each image and ensemble averaging over the entire sequence of 508 images. Microscales in the vertical direction, shown as squares, are consistently larger than microscales in the horizontal direction, shown as triangles. This evidence of longer length scales in the vertical than in the horizontal direction is consistent with the indications of the power spectra (Sec. 5), and directional PDFs of scalar increments (Sec. 7). Figure 24 also plots the ratio of horizontal to vertical microscales as a function of Reynolds number. The anisotropy of the scalar microscale initially increases with increasing Reynolds number, then decreases for jet Reynolds numbers $Re_{\rm j} \geq 10 \times 10^3$. The scalar microscale increases with Reynolds number, up to $Re_{\rm j} = 10 \times 10^3$, and begins to decrease with further increases in Reynolds number. In the limit of very large Reynolds numbers, the scalar microscale, referenced to the outer scale, is expected to decrease as the square root of the local Reynolds number based on the outer scale. This is not observed here. Higher Reynolds numbers than those attained in this experiment may be necessary to draw conclusions about the asymptotic behavior of scalar microscales.

The precision in determining the mean scalar microscales, $\lambda_{C,z}$ and $\lambda_{C,y}$, is indicated by the error bars in Fig. 24. These error bars, which are of size equal to two standard deviations of the mean, are smaller than the size of the plot symbols

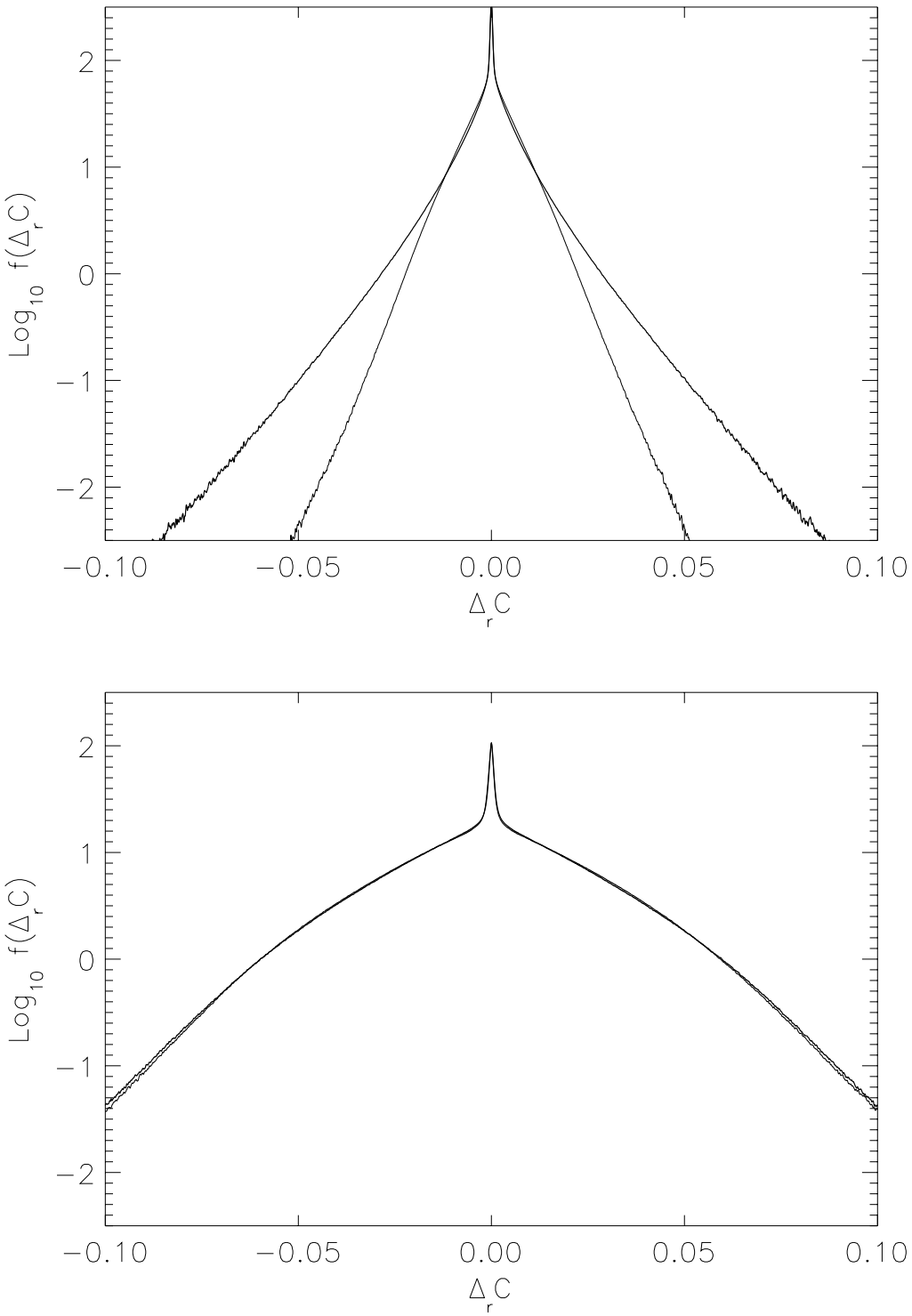

FIG. 22 PDFs of scalar increments for the same horizontal and vertical separations. $Re_{\rm j} = 2.0 \times 10^3$ and $x/d_{\rm j} = 50$. Top: Outer PDF is for horizontal separations of $\mathbf{r}/\delta_{\rm h} = 2.2 \times 10^{-3}\,\widehat{\mathbf{z}}$, and inner PDF is for vertical separations of $\mathbf{r}/\delta_{\rm h} = 2.2 \times 10^{-3}\,\widehat{\mathbf{y}}$. Bottom: $\mathbf{r}/\delta_{\rm h} = 17 \times 10^{-3}\,\widehat{\mathbf{z}}$ and $17 \times 10^{-3}\,\widehat{\mathbf{y}}$.

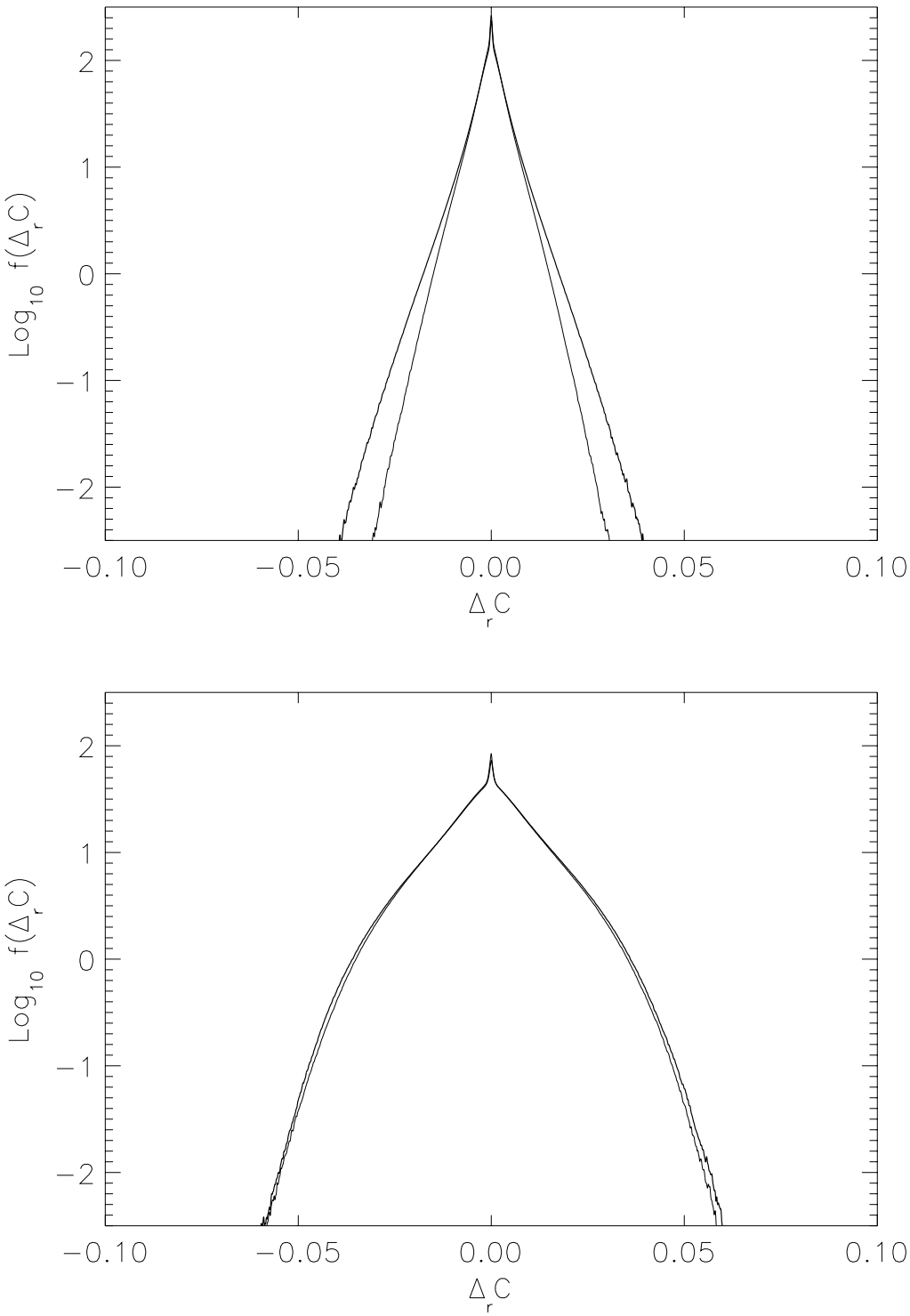

FIG. 23 Same as Fig. 22, but for $Re_{\rm j} = 20 \times 10^3$. Top: Outer PDF is for horizontal separations of $\mathbf{r}/\delta_{\rm h} = 2.5 \times 10^{-3}\,\widehat{\mathbf{z}}$, and inner PDF is for vertical separations of $\mathbf{r}/\delta_{\rm h} = 2.5 \times 10^{-3}\,\widehat{\mathbf{y}}$ pixels. Bottom: $\mathbf{r}/\delta_{\rm h} = 20 \times 10^{-3}\,\widehat{\mathbf{z}}$ and $20 \times 10^{-3}\,\widehat{\mathbf{y}}$.

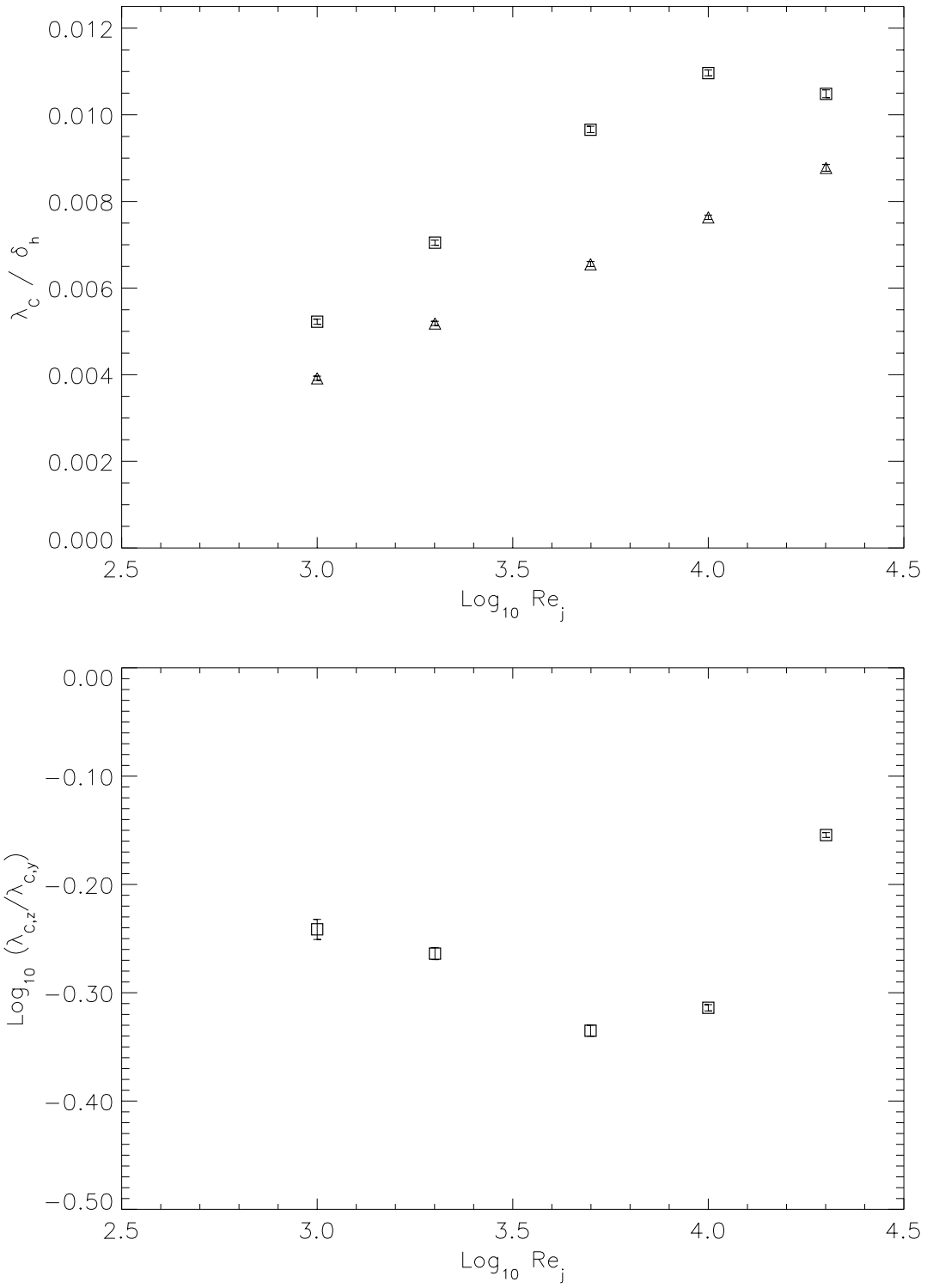

FIG. 24 Scalar microscale as a function of jet Reynolds number. Length scale is pixels, and error bars are smaller than plot symbols for all but lowest-Reynolds-number case. Left: Scalar microscale. Squares and triangles denote microscale in the vertical and horizontal directions, respectively. Right: Ratio of horizontal to vertical microscales.

in all cases. The standard deviation of the mean microscale is computed as

$$\sigma_{<\lambda_{C,i}>} \equiv \sqrt{\frac{1}{N(N-1)} \sum_{n=1}^{N} \left(\lambda_{C,i} - \langle \lambda_{C,i} \rangle\right)^2}, \tag{21}$$

where N = 508, the number of images at each Reynolds number. Error bars for the ratio of horizontal-to-vertical length scales, $\lambda_{C,z}/\lambda_{C,y}$, are computed in similar fashion. They also are smaller than the plotted symbols, for all but the lowest Reynolds number, $Re_{\rm j} = 1.0 \times 10^3$. The error bars on the mean microscales, $\lambda_{C,i}$, and the mean anisotropy ratio, $\lambda_{C,z}/\lambda_{C,y}$, are an indication of the precision, rather than the accuracy, of the measurement.

9. Anisotropy of the scalar field

The scalar field of the transverse jet is anisotropic, even at small length scales. Evidence for this was seen in the one- and two- dimensional power spectra (Sec. 5), the directional PDF of scalar increments (Sec. 7), and the directional scalar microscales (Sec. 8). This small-scale anisotropy of the scalar field is believed to be a consequence of the global dynamics of the transverse jet. In particular, a counter-rotating vortex pair dominates the flow in the far field of the transverse jet. This vortex pair induces a vertically-aligned mean strain field, which stretches scalars in the upper-half of the jet cross-section. The strain field, acting on the scalar field, produces thin, vertical filaments, or "fingers," in the wake of the jet. As a result, the anisotropy is localized to specific regions of the transverse jet. Evidence for this is seen in Fig. 25, which shows the scalar microscale computed for small sections of the transverse jet. Crosses representing the scalar microscales, $\lambda_{C,i}$, in each direction are superimposed on an image of the ensemble-averaged, jet-fluid-concentration field at $x/d_{\rm j} = 50$, for $Re_{\rm j} = 20 \times 10^3$. The crosses have horizontal and vertical dimensions that are $4\lambda_{C,z}$ and $4\lambda_{C,y}$, respectively. The anisotropy of the scalar fluctuations is greatest in the upper half of the image, particularly in the region between the vortex centers. This is precisely the area where extensional strain produced by the counter-rotating vortex pair is greatest. We infer from this that anisotropic, large-scale flow can impose itself on the small-scale features of the scalar field.

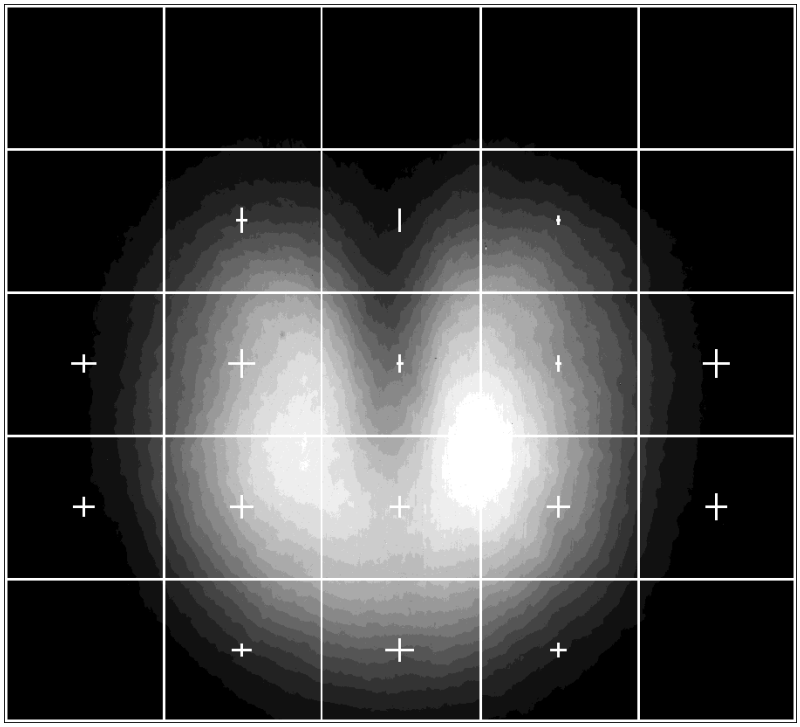

FIG. 25 Localized scalar microscale for $Re_j = 20 \times 10^3$. Microscales are computed in each rectangular section shown, and ensemble averaged over 508 images. Horizontal and vertical dimensions of the crosses are $4\lambda_{C,z}$ and $4\lambda_{C,y}$, respectively.

Local anisotropy of the scalar field has been found in other flows. By local isotropy, the scalar derivative skewness, or equivalently, the third-order scalar structure function in the limit of vanishing separation distance, is expected to be zero. Yet, if a mean scalar gradient is imposed on a flow, the scalar derivative skewness is found to be finite even at the highest Reynolds numbers at which measurements are available today (Sreenivasan 1991). Tong & Warhaft (1994) and Mydlarski & Warhaft (1998) found scalar anisotropy in isotropic grid turbulence with an superimposed mean temperature gradient. Similar results have been found for homogenous shear flows, wakes, and atmospheric boundary layers (Sreenivasan & Antonia 1997). The numerics of Holzer & Siggia (1994) demonstrated that, even with a Gaussian, homogeneous, isotropic velocity field, a mean superimposed scalar gradient can cause scalar anisotropy and finite derivative skewness. However, for the transverse jet, there is left-right and top-bottom symmetry in the scalar fields for transverse slices. Thus, anisotropy manifests itself not in the odd-ordered structure functions but in other ways, *e.g.*, the spectra, directional PDF of scalar increments,

and the directional scalar microscales. In this sense, the scalar anisotropy of the transverse jet is different from that found in most previous work.

10. Conclusions

Reynolds number effects and flow dependence of PDF of scalar concentration — Enhanced scalar mixing (better spatial homogenization) with increasing Reynolds number is found in experimental investigations of liquid-phase transverse jets in the range $1.0 \times 10^3 \leq Re_j \leq 20 \times 10^3$. Classical measures of the jet, such as scalar trajectory and maximum mean-concentration decay, are seen to be independent of Reynolds number. However, the probability density function of jet-fluid-concentration evolves with Reynolds number. In the far field of the transverse jet, the scalar PDF evolves from a monotonically-decreasing function to a strongly-peaked distribution with increasing Reynolds number. The behavior of the PDF is explained as a consequence of the competition between entrainment, stirring, and molecular mixing. Turbulent mixing is seen to be flow dependent, based on the difference between the trends with increasing Reynolds number for the transverse jet, and the jet discharging into a quiescent reservoir.

Scalar increment PDF — Using a novel technique for whole-field computation of scalar differences, PDFs of scalar differences in the transverse jet are found to tend toward exponential-tailed distributions with decreasing separation distance. These long-tailed PDFs of scalar differences are found despite the inhomogeneity, anisotropy, and non-Gaussian distribution of the scalar field in the transverse jet. This result is consistent with investigations in grid-turbulence, Rayleigh-Benard convection, and other turbulent flows.

Anisotropy of scalar field — The scalar field is seen to be inhomogeneous and anisotropic with decreasing scale. Power spectra of jet-fluid concentration in the far field of the jet are found to be isotropic for low wavenumbers, and increasingly anisotropic for higher wavenumbers. This anisotropy at small scales is also reflected in the directional dependence of the PDF of scalar increments. PDFs of scalar increments are narrower for small, vertical increments than for small, horizontal increments. The scalar field has less variation (in terms of distributions of scalar increments, and scalar structure functions) in the vertical direction than in the horizontal direction. The small-scale anisotropy of the scalar field persists from the lowest Reynolds numbers investigated, $Re_j = 1.0 \times 10^3$, to the highest Reynolds

numbers studied, $Re_j = 20 \times 10^3$. Further evidence for the anisotropy of the scalar field is also seen in the directional dependence of the scalar microscales. The observed, small-scale, anisotropy of the scalar field is believed to be a consequence of mean strain field produced by the dominant, kidney-shaped vortex pair in the transverse jet. The anisotropic, large-scale flow imposes itself on even the smallest features of the scalar field.

11. Acknowledgements

We would like to acknowledge assistance by D. Lang with the Cassini digital imaging system and P. Svitek for assistance with mechanical design and the operation of the GALCIT Free-Surface Water Tunnel. We would also like to acknowledge discussions with D. Pullin, and helpful comments by M. Gharib, H. Hornung, A. Leonard, and Z. Warhaft. This research was supported by the Air Force Office of Scientific Research, under grants F49620–98–1–0052 and F49620–01–1–0006, and a NDSEG fellowship. Development of the Cassini digital imaging system was additionally supported by DURIP grant F49620–95–1–0199, and AFOSR grants F49620–94–1–0283 and F49620–00–1–0036.

Appendix: PDFs for higher-dimensional distributions

The PDF for a distribution, $C(\mathbf{r})$, in d-dimensional space is the differential d-dimensional volume, $\mathrm{d}V_d(C)$, associated with a differential concentration, $\mathrm{d}C$,

$$f_d(C) \;=\; \frac{1}{V_{d,\mathrm{tot}}} \left| \frac{\mathrm{d}V_d(C)}{\mathrm{d}C} \right| \;. \tag{15b}$$

Normalization by the total volume, $V_{d,\mathrm{tot}}$, is necessary so that the PDF has the properties discussed in Sec. 6, and proper dimensions, $1/C$.

Consider, for instance, the Gaussian scalar distribution,

$$C(r,t) \;=\; \frac{1}{2^d(\pi\mathcal{D}t)^{d/2}}\, e^{-r^2/4\mathcal{D}T} \;=\; \frac{1}{(2\pi)^{d/2}\sigma^d}\, e^{-r^2/2\sigma^2} \;. \tag{22}$$

This is the solution to the d-dimensional initial-value problem for the diffusion equation on an infinite domain with initial conditions of a delta function at the origin, $C(\mathbf{r}, t=0) = \delta(\mathbf{r})$. Here, $\sigma^2 = 2\mathcal{D}t$. The differential length, $\mathrm{d}r$, at any given time (*i.e.*, σ =constant) is related to $\mathrm{d}C$ by

$$\frac{\mathrm{d}r}{\mathrm{d}C} \;=\; -\frac{(2\pi)^{d/2}\sigma^d}{2r}\, e^{r^2/2\sigma^2} \;. \tag{23a}$$

Using (22), $\mathrm{d}r/\mathrm{d}C$ can be written as a function of C alone:

$$\frac{\mathrm{d}r}{\mathrm{d}C} \;=\; \frac{1}{2\,C\,r} \;=\; \frac{1}{2\sigma C\left\{-2\ln\left[\,(2\pi)^{d/2}\sigma^{d}C\,\right]\right\}^{1/2}}\;. \tag{23b}$$

The differential d-dimensional volume $\mathrm{d}V_d(C)$ may then be expressed as a function of C using (22) and (23) to yield the form of the PDF for a d-dimensional Gaussian distribution:

$$f_d(C) \;\propto\; \frac{[\,\ln(1/C)\,]^{d/2-1}}{C}\;. \tag{24}$$

For one-, two-, and three-dimensional Gaussian concentration distributions, the PDFs are then:

$$f_1(C) \;\propto\; \frac{1}{C\,[\,\ln(1/C)\,]^{1/2}}\;. \tag{24a}$$

$$f_2(C) \;\propto\; \frac{1}{C}\;. \tag{24b}$$

$$f_3(C) \;\propto\; \frac{[\,\ln(1/C)\,]^{1/2}}{C}\;. \tag{24c}$$

These functions are shown in Fig. 26. The distribution for the one-dimensional case has two peaks, at $C = 0$ and $C = 1$, while the distributions for the two- and three-dimensional cases each have a peak at $C = 1$. The PDF decreases monotonically to zero at C=1 for the three-dimensional Gaussian, and to a nonzero minimum for the two-dimensional Gaussian.

Since d-dimensional transects of a higher-dimensional Gaussian are themselves d-dimensional Gaussians, the PDFs above can be viewed as PDFs of concentration distributions in d-dimensional space, or as d-dimensional measurements of a higher-dimensional distribution. Thus, a PDF can depend on the dimensionality of the space (or measurement), as well as the concentration field, $C(\mathbf{r})$.

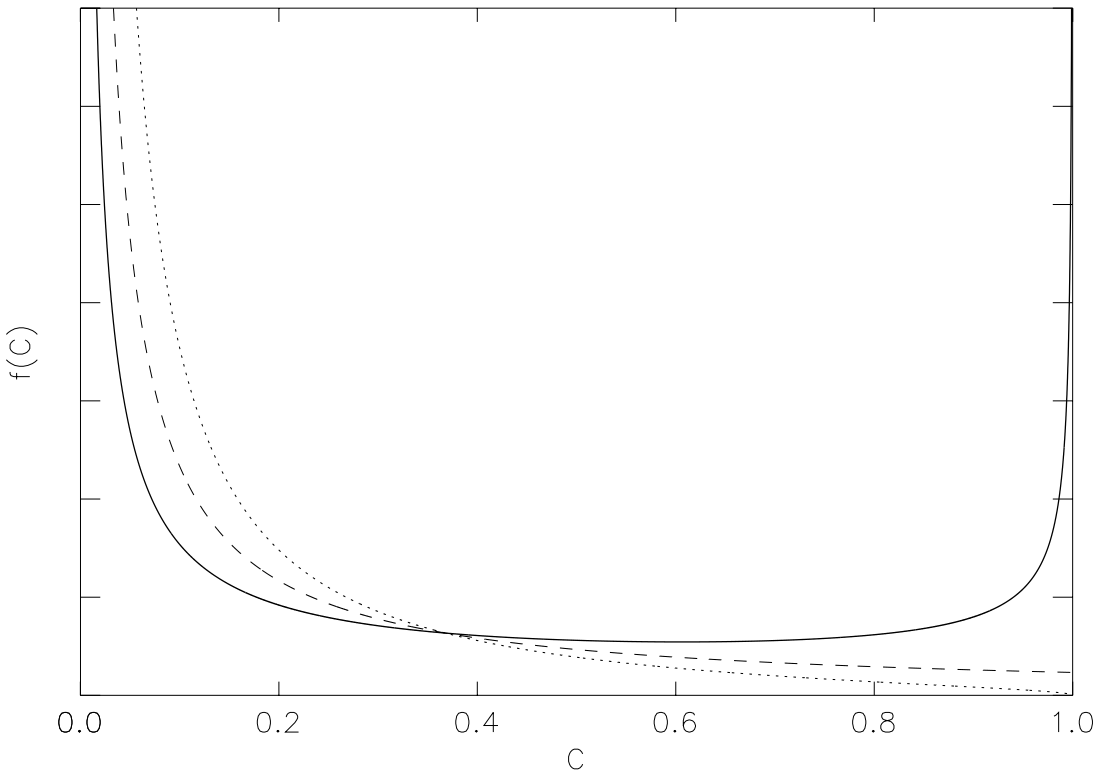

FIG. 26 PDFs of diffusive (Gaussian) distributions. Solid line: one-dimensional. Dashed line: two-dimensional. Dotted line: three-dimensional.

References

ALISSE, J. R. & SIDI, C. 2000 Experimental probability density functions of small-scale fluctuations in the stably stratified atmosphere. *J. Fluid Mech.* **402**, 137–162.

ANDREOPOULOS, J. & RODI, W. 1984 An experimental investigation of jets in a crossflow. *J. Fluid Mech.* **138**, 93–127.

ANTONIA, R. A., BROWNE, L. W. B., BRITZ, D. & CHAMBERS, A. J. 1984 A comparison of properties of temporal and spatial temperature increments in a turbulent plane jet. *Phys. Fluids* **27**(1), 87–93.

AXELROD, D., KOPPEL, D. E., SCHLESSINGER, J., ELSON, E. & WEBB, W. W. 1976 Mobility measurement by analysis of fluorescence photobleaching recovery kinetics. *Appl. Phys. Lett* **16**, 1055–1069.

BROADWELL, J. E. & BREIDENTHAL, R. E. 1984 Structure and mixing of a transverse jet in incompressible flow. *J. Fluid Mech.* **148**, 405–412.

Chassaing, P., George, J., Claria, A. & Sananes, F. 1974 Physical characteristics of subsonic jets in a cross-stream. *J. Fluid Mech.* **62**, 41–64.

Ching, E. S. C. 1991 Probabilities for temperature differences in Rayleigh-Benard convection. *Phys. Rev.* A **44**, 3622–3629.

Cook, A. W. & Dimotakis, P. E. 2000 Transition stages of Rayleigh-Taylor instability between miscible fluids. *J. Fluid Mech.* **443**, 69–99.

Corrsin, S. 1951 On the spectrum of isotropic temperature fluctuations in isotropic turbulence. *J. Appl. Phys.* **22**, 469–473.

Cortelezzi, L. & Karagozian, A. R. 2001 On the formation of the counter-rotating vortex pair. Submitted to *J. Fluid Mech.* .

Dimotakis, P. E. 1986 Two-Dimensional Shear-Layer Entrainment. *AIAA J.* **24**, 1791–1796.

Dimotakis, P. E. 2000 The mixing transition in turbulence. *J. Fluid Mech.* **409**, 69–98.

Dimotakis, P. E. & Catrakis, H. J. 1996 Turbulence, fractals, and mixing. NATO Advanced Studies Institute series, *Mixing: Chaos and Turbulence*, GALCIT Report FM97–1.

Eckart, C. 1948 An Analysis of the Stirring and Mixing Processes in Incompressible Fluids. *J. Marine Research* **VII**, 265–275.

Fearn, R. & Weston, R. P. 1974 Vorticity associated with a jet in a cross flow. *AIAA J.* **12**, 1666–1671.

Fric, T. F. & Roshko, A. 1994 Vortical structure in the wake of a transverse jet. *J. Fluid Mech.* **279**, 1–47.

Frisch, U. 1995 *Turbulence. The Legacy of Kolmogorov*. Cambridge U.P., Cambridge U.K..

Gargas, D. 2000 Photochemical decomposition studies of fluorescein dye. Summer Undergraduate Research Fellowship report, California Institute of Technology (unpublished).

Goldin, G. M. & Menon, S. 1997 A scalar PDF construction model for turbulent non-premixed combustion. *Combust. Sci. and Technol.* **125**, 47–72.

Gordier, R. L. 1959 Studies on fluid jets discharging normally into moving liquid. St. Anthony Falls Hyd. Lab., U. Minnesota, Tech. Paper No. 28, Series B.

Guilkey, J. E., Kerstein, A. R., McMurtry, P. A. & Klewicki, J. C. 1997 Long-tailed probability distributions in turbulent-pipe-flow mixing. *Phys. Rev*. E, **56**(2), 1753–1758.

Holzer, M. & Siggia, E. D. 1994 Turbulent mixing of a passive scalar. *Phys. Fluids* **6**(5), 1829–2176.

Jayesh & Warhaft, Z. 1992 Probability distributions, conditional dissipation, and transport of passive temperature fluctuations in grid-generated turbulence. *Phys. Fluids* **4**(10), 2292–2307.

Kailasnath, P., Sreenivasan, K. R. & Saylor, J. R. 1993 Conditional scalar dissipation rates in turbulent wakes, jets, and boundary layers. *Phys. Fluids* A, **5**(12), 3207–3215.

Kamotani, Y. & Greber, I. 1972 Experiments on a turbulent jet in a cross flow. *AIAA J*. **10**(11), 1425–1429.

Karagozian, A. R. 1986 An analytical model for the vorticity associated with a transverse jet. *AIAA J*. **24**(3), 429–436.

Karasso, P. S. & Mungal, M. G. 1997 PLIF measurements in aqueous flows using the Nd:YAG laser. *Exps. in Fluids* **23**, 382–387.

Keffer, J. F. & Baines, W. D. 1963 The round turbulent jet in a cross-wind. *J. Fluid Mech*. , **15**, 481–496.

Kelso, R. M., Lim, T. T. & Perry, A. E. 1996 An experimental study of round jets in cross-flow. *J. Fluid Mech*. **306**, 111–144.

Kelso, R. M. & Smits, A. J. 1995 Horseshoe vortex systems resulting from the interaction between a laminar boundary layer and a transverse jet. *Phys. Fluids* **7**(1), 153–158.

Kolmogorov, A. N. 1941 Local Structure of Turbulence in an Incompressible Viscous Fluid at Very High Reynolds Numbers. *Dokl. Akad. Nauk SSSR* **30**, 301–305.

Kuznetsov, V. R. & Sabel'nikov, V. A. 1990 *Turbulence and Combustion*. Hemisphere Publishing, New York.

Kuzo, D. M. 1995 *An Experimental Study of the Turbulent Transverse Jet*. Ph.D. Thesis, California Institute of Technology, Pasadena, CA.

Kuzo, D. M. 1995 *An Experimental Study of the Turbulent Transverse Jet*. Ph.D. Thesis, California Institute of Technology, Pasadena, CA.

Kuzo, D. M. & Roshko, A. 1984 Observations on the wake region of the transverse jet. *Bull. Am. Phys. Soc.* **29**, 1536.

Margason, R. J. 1993 Fifty Years of Jet in Cross Flow Research. AGARD Meeting on Computational and Experimental Assessment of Jets in Cross Flow, April, 1993.

McAllister, J. D. 1968 *A momentum theory for the effects of cross flow on incompressible jets*. Ph.D. thesis, University of Tennessee.

McMahon, H. M., Hester, D. D. & Palfery, J. G. 1971 Vortex Shedding from a Turbulent Jet in a Cross-Wind. *J. Fluid Mech.* **48**, 73–80.

Morton, B. R. & Ibbetson, A. 1996 Jets Deflected in a Crossflow. *Exp. Thermal and Fluid Sc.* **12**, 112–133.

Moussam Z. M., Trischka, J. W. & Eskinazi, S. 1977 The near field in the mixing of a round jet with a cross-stream. *J. Fluid Mech.* **80**, 49–80.

Mydlarski, L. & Warhaft, Z. 1998 Three-point statistics and the anisotropy of a turbulent passive scalar. *Phys. Fluids* **10**(11), 2885–2894.

Niederhaus, C. E., Champagne, F. H. & Jacobs, J. W. 1997 Scalar Transport in a Swirling Transverse Jet. *AIAA J.* **35**, 1697–1704.

Oboukhov, A. M. 1949 Structure of the temperature field in turbulent flows. *Izv. Ak. Nauk SSR, Geogr. & Geophys. Ser.* **13**, 58–69.

Ould-Rouis, M., Anselmet, F., Le Gal, P. & Vaienti, S. 1995 Statistics of temperature increments in fully developed turbulence Part II. Experiments. *Physica* D **85**, 405–424.

Pope, S. B. 1985 PDF Methods for Turbulent Reactive Flows. *Prog. Energy Comb. Sc.* **11**, 119–192.

Pratte, B. D. & Baines, M. 1967 Profiles of the round turbulent jet in a crossflow. *J. Hydronaut. Div. ASCE* **92**, 53–64 .

Pringsheim, P. 1949 *Fluorescence and phosphorescence*. Interscience Publishers, Inc.

Reilly, R. S. 1968 *Investigation of the deformation and penetration of a turbulent subsonic jet issuing transversely into a uniform, subsonic main stream*. Ph.D. thesis, University of Maryland.

Richardson, L. F. 1922 *Weather Prediction by Numerical Process*. Cambridge U. P..

Shan, J. W., Lang, D. B. & Dimotakis, P. E. 2001 Suitability of rhodamine-6G chloride and the Q-switched, Nd:YAG laser for scalar concentration measurements. (in preparation).

Shraiman, B. & Siggia, E. 2000 Scalar turbulence. *Nature* **405**, 639–646.

Smith, S. H. & Mungal, M. G. 1998 Mixing, structure and scaling of the jet in crossflow. *J. Fluid Mech.* **357**, 83–122.

Sreenivasan, K. R. 1991 On local isotropy of passive scalars in turbulent shear flows. *Proc. Roy. Soc. London* A **434**, 165–182.

Sreenivasan, K. R. & Antonia, R. A. 1997 The phenomenology of small-scale turbulence. *Ann. Rev. Fluid Mech.* **29**, 435–472.

Tennekes, H. & Lumley, J. L. 1972 *A First Course in Turbulence*. MIT Press.

Tong, C. & Warhaft, Z. 1994 On passive scalar derivative statistics in grid turbulence. *Phys. Fluids* **6**(6), 2165–2176.

Walker, D. A. 1987 A fluorescence technique for measurement of concentration in mixing liquids. *J. Psys. E.: Sci. Instrum.* **20**, 217–224.

Warhaft, Z. 2000 Passive scalars in turbulent flows. *Ann. Rev. Fluid Mech.* **32**, 203–240.

Yuan, L. L., Street, R. L. & Ferziger, J. H. 1999 Large-eddy simulations of a round jet in crossflow. *J. Fluid Mech.* **379**, 71–104.